Growth and development of spring towers at Shiqiang, Yunnan Province, China

Brian Jones[a], Xiaotong Peng[b]

[a] *Department of Earth and Atmospheric Sciences, University of Alberta, Edmonton, T6G 2E3, Canada*

[b] *Institute of Deep-Sea Science and Engineering, Chinese Academy of Science, Sanya, 572000, China*

E-mail address: Brian.Jones@ualberta.ca

Abstract

Throughout the world, high artesian pressures in hydrothermal areas have led to the growth of tall spring towers that have their vents at their summits. The factors that control their development and formative precipitates are poorly understood because these springs, irrespective of location, are mostly inactive. Spring towers found at Shiqiang (Yunnan Province, China), which are up to 4 m high and 3 m in diameter, are formed largely of calcite and aragonite crystal bushes, euhedral calcite crystals and coated grains with alternating Fe-poor and Fe-rich zones, calcite rafts, and cements formed of various combinations of calcite, aragonite, strontianite, Mg-Si reticulate, needle fiber calcite, calcified and non-calcified microbes, diatoms, and insects. Collectively, the limestones that form the towers can be divided into (1) Group A that are friable, porous and form the cores of the towers and have $\delta^{18}O_{SMOW}$ values of +15.7 to +19.7‰ (average 17.8‰) and $\delta^{13}C_{PDB}$ values of +5.1 to +6.9‰ (average 5.9‰), and (2) Group B that are hard and well lithified and found largely around the vents and the tower sides, and have $\delta^{18}O_{SMOW}$ values of +13.0 to +22.0‰ (average 17.6‰) and $\delta^{13}C_{PDB}$ values of +1.4 to +3.6‰ (average 2.6‰). The precipitates and the isotopic values indicate that these were thermogene springs. Growth of the Shiqiang spring towers involved (1) Phase IA when precipitation of calcite and aragonite bushes formed the core of the tower and Phase IB when calcite, commonly Fe-rich, was precipitated locally, (2) Phase II that involved the precipitation of white cements, formed of calcite, aragonite, strontianite, and Mg-Si reticulate coatings in cavities amid the Phase I precipitates, and (3) Phase III, which formed probably after spring activity ceased, when needle-fibre calcite was precipitated and the mounds were invaded by microbes (some now calcified), diatoms, and insects. At various times during this complex history, pore waters mediated dissolution of the calcite and aragonite and sometimes partial alteration of the aragonite. The diverse array of

precipitates, depositional fabrics and diagenetic changes clearly indicate that the composition of the spring water changed frequently. Growth of the spring towers at Shiqiang continued until there was insufficient artesian pressure to lift the water above the top of the tower vent.

Keywords: Hot springs, calcite, aragonite, opal-A, isotopes, dendrites

1. Introduction

Hydrothermal landscapes associated with hot springs are commonly characterized by a diverse array of landforms that have developed as $CaCO_3$ was precipitated from the spring waters. Among the rarest and most spectacular landforms are towers that have a height that is greater than their diameter and have their vent at the apex. Examples include Liberty Cap and Devil's Thumb in the Mammoth Hot Spring complex (Bargar, 1978, his Fig. 8; Chafetz and Guidry, 2003, their Fig. 2C; Jettestuen et al., 2006, their Fig. 9b; Meakin and Jamtveit, 2010, their Fig. 9), and those in the Travertine Totem Forest in Yellowstone National Park (Hutchinson and Thompson, 1992), the Jifei spring complex in Yunnan Province, China (Liu et al., 2012, their Fig. 3), the Rongma hot spring complex in Tibet (Gao et al., 2013, their Figs. 2A, 3B), the Chaga, Zhi-A, and Longma'er Travertine Stone Forest of Tibet (Dunzhujiacan and Wu, 1985, their Figs. 123, 127, and 128), and the Shiqiang in Yunnan Province, China (Jones and Peng, 2014a, their Fig. 2). In the context of hydrothermal spring systems, these enigmatic structures are unique because they grew when artesian pressures were high and vertical growth outpaced lateral accretion. Determination of the processes involved in the development of these structures is handicapped by the fact that none of these tower springs is active today. For example, when Liberty Cap in Yellowstone National Park was discovered and named in 1871, it was illustrated and described as having no water flowing from it (Hayden, 1872, his Fig. 14 and p. 67). The problem is compounded by the fact that many of these structures occur in protected areas where sampling is not allowed and vertical cross-sections through these towers are non-existent. Thus, the manner in which these structures grew is open to debate even though Jettestuan et al. (2006, their Fig. 10) and Meakin and Jamtveit (2016, their Fig. 9a, b) developed mathematical models to explain the growth of Liberty Cap.

At Shiqiang, located in Yunnan Province, China (Fig. 1), there are numerous inactive spring towers that are up to 4 m high (Figs. 2, 3). Although most are located in a protected tourist area and could not be examined in detail or sampled (Fig. 2), three towers in farmland to the southeast were accessible in 2013. Using samples collected from these three towers, this study (1) describes the precipitates involved in their construction, (2) derives the isotopic signatures of the precipitates, and (3) establishes the different phases of development involved in the growth of the towers. Integration of this information provides the basis for establishing, for the first time, a multifaceted examination of the evolution of spring towers. As such, it should provide an evolutionary model against which other spring towers can be compared.

2. General Setting

Shiqiang is located at 25° 21’ 40.11” N and 98° 37’ 51.24”, 8 km SSW of Jietou, in a rural part of Yunnan Province (Fig. 1) that is characterized by extensive farmland but little bedrock exposure. The springs at Shiqiang (also known as Stone Wall) are located on the Longchuanjiang Fault that cuts through the Tengchong block that resulted from the collision of the Indian and Eurasian plates (Du et al., 2005). Located on the east margin of the Tibet-Yunnan geothermal zone (Kearey and Wei, 1993), faulting and volcanic activity affected this block until the early Cenozoic (Zhu and Tong, 1987; Du et al., 2005).

Shiqiang includes (1) two active hot springs, with no evidence of tower development (Jones and Peng, 2016), and (2) inactive spring towers, of variable shape and size, that are up to 4 m high and up to 3 m in diameter (Fig. 1C). Fourteen inactive spring towers are located in small, fenced lakes (Fig. 2) in the northwest part of the area that used to be open to tourists. South of the two active springs there are three spring towers in a farmer’s field (Fig. 3).

The climate of Shiqiang is similar to that for Tengchong, which is located 32 km to the

SSW (Fig. 1B). Climate records between 1971 and 2000 showed that the subtropical highland climate of the Tengchong area had an average annual rainfall of 1480 mm and annual mean temperature of 14.9°C. The seasonal climate ranges from temperatures of 1 to 17°C, rainfall of 73 mm, and 244 hours of sunshine in January to temperatures of 17 to 24°C, rainfall of 286 mm, and 73 hours of sunshine in June (see Jones and Peng, 2012, their Fig. 3). The low hours of sunshine during June is due to the cloud cover associated with the heavy monsoonal rains.

3. Methodology

The 14 spring towers located in the lakes in the northwest part of the site (Fig. 1C) could not be sampled because they are part of the protected tourist site. Thus, sampling was limited to the three spring towers (ST1, ST2, ST3) located in the farmland to the southeast of the two active springs (S1 and S2 – Fig. 1C). One tower (ST1 – Fig. 1C) was in very good condition (Fig. 3A), one tower (ST2 – Fig. 1C) was in poor to moderate condition (Fig. 3B), and the third tower (ST3 – Fig. 1C) had been largely destroyed with only its basal part remaining. Although sampling was focused largely on ST1, some samples were also collected from ST2 and ST3. Today, the main vents (~ 0.3 m diameter) of ST1 and ST2, located at the top of the towers (Fig. 2B), are filled with soil and actively growing grasses (ST1 – Fig. 3A) and trees (ST2 – Fig. 3B). Actively growing mosses and grasses are also found on the sides of the towers (Fig. 3A, B). Although sampling was allowed in May, 2013, a change in land ownership meant that access was impossible when the site was revisited in 2015.

Oriented samples were collected from ST1 in order to obtain a comprehensive set of the formative lithologies. Fewer samples were collected from ST2 and ST3 because they are not as well preserved. The large scale fabrics of the samples were established from 23 large (7 x 5 cm) thin sections that were produced after the samples had been impregnated with blue epoxy.

Small fracture samples (~ 1 cm^3) were extracted from the larger samples for examination on the scanning electron microscope (SEM). After mounting on a SEM stub, each sample was sputter coated with gold or carbon before being examined on a JEOL 6400FE SEM with an accelerating voltage of 5 kV. Crystal morphology and elemental composition as determined by Energy-dispersive X-ray (EDX) analyses, which were done with an accelerating voltage of 20 kV, were used to identify the minerals evident on the SEM. The average spot size of ~ 1 μm was used for the EDX analyses and numerous analyses were done to verify the presence of the detected elements.

Assessment of the samples was based on detailed petrographic analysis of the thin sections and 4034 SEM photomicrographs that were obtained from 30 different SEM samples. The grey levels and contrast of some SEM images were modified using PhotoShop CC©. A black background was introduced into some images in order to accentuate the main features of the sample.

Twenty-four samples, each ~ 1 g, were taken from various parts of the hand samples and ground into a powder using a mortar and pestle. The mineralogy of these samples was determined by X-ray diffraction (XRD) analyses that used a Rigaku Ultima IV Powder XRD system that was run at 38 kV and 38 mA using an Ultima IV X-ray generator with a Co tube. All scans were run from 5° to 90° 2θ at a speed of 2° θ/min. Once the mineralogy had been established, the same samples were used for stable isotope analyses. The percentages of calcite and aragonite were determined from the XRD analyses by using the equation $y = 56.2982x^3 - 1.1170x^2 + 45.2572x$ in which y = % calcite and $x = d_{104}/(d_{104} + d_{111} + d_{021})$ with the d values being the peak heights. This equation, derived by Dr. A. Locock (pers. comm., Electron Microprobe Laboratory, University of Alberta) is based on artificial samples created with known

percentages of calcite and aragonite, is the same equation used by Li and Jones (2014). The values obtained by this method are accurate at ±2 wt%.

The isotope analyses, undertaken by Isotope Tracer Technologies Inc. (Ontario, Canada), are reported in the Vienna-Pee Dee Belemnite (VDPB) notation. After being flushed with helium for 4 min, the samples were dried in an oven for 15 min at a temperature of 50°C and then acidified with four drops of 100% phosphoric acid. After 2 hours of reaction time, aliquots were injected into a HP6890 GC-C + Delta Plus XL IRMA system for analysis (Hewlett Packard Company, Palo Alto, California, USA). The standards, NIST-19, NIST-18 and IT2-21, were run every five samples. The reproducibility is 0.15‰ for $\delta^{18}O_{(calcite)}$ and 0.1‰ for $\delta^{13}C_{(calcite)}$.

4. Terminology

A wide variety of descriptive terms have been used for deposits that are localized around spring vents. These include, for example, "mounds" (e.g., Pentecost, 2005, his Fig. 10), "cone-type hot spring" and "hot spring cones" (Bargar, 1978, his Fig. 8), "well-developed cone-shaped accumulation" (Chafetz and Guidry, 2003, their Fig. 2C), "travertine cones" (Hutchinson and Thompson, 1992; Liu et al., 2012, their Fig. 3; Gao et al., 2013, their Fig. 3A), "spring towers" (Jones and Peng, 2014a, 2014c), "travertine mounds" or "travertine chimneys" (Houssein, 2010; Houssein et al., 2013), and "towers" (Kempe et al., 1991; Guo and Chafetz, 2012). These terms encompass a wide range of morphological structures that have developed on land, partly submerged in water, or completely underwater. Herein the term *spring tower* is applied to those spring-generated structures that have (1) their main vent at the top of the structure, and (2) are of limited areal extent with no associated discharge apron. Although the height of the structure is typically greater than the diameter, this is not always the case. The use of the term "cone" is avoided because (1) the height of a cone does need not be greater than its diameter, and (2) many

of the highest structures of this type have (sub)parallel sides with any hint of a "cone" shape being evident only in the uppermost part of the structure.

From the perspective of the location where these structures formed, they can be referred to as "terrestrial spring towers" if they form on land, "submerged spring towers" if their development was completely underwater, and "partly submerged spring towers" if the basal part of the tower was submerged and the upper part (including the spring vent) was above water level.

5. Results

The spring towers at Shiqiang are ~ 0.5 m (Fig. 2A) to ~ 4.0 m (Fig. 3A) high with an external morphology that ranges from conical (Fig. 2B), to mushroom-shaped (Fig. 2C), to forms with parallel sides and a conical upper part (Fig. 3A), to mounds (diameter > height) that may have been formed by the merging of two or more smaller towers (Fig. 2A). There is no pattern to the distribution of the different morphological forms as towers that are side-by-side and only a few meters apart may be significantly different (Fig. 2). All of the spring towers at Shiqiang are now inactive with various plants (e.g., grasses, trees) growing in the soils that fill their vents (Fig. 2, 3). The sides of the towers are weathered and largely covered by moss and other plants (Figs. 2, 3).

Information derived from the field, thin section, and SEM indicates that the deposits in these enigmatic structures can be divided into (1) Phase I that includes all of the original precipitates that led to the initial growth and formation of the towers, (2) Phase II that includes the white precipitates (Fig. 3C, D) that were precipitated in the cavities in the Phase I precipitates, and (3) Phase III that includes needle fiber calcite (Jones and Peng, 2014a) and calcified cyanobacteria (Jones and Peng, 2014c).

5.1. Phase I

Phase I included (1) growth of complex crystal bushes, formed of calcite and aragonite, (2) precipitation of Fe-rich limestones that include Fe-rich laminae and Fe-dendrites, (3) precipitation of zoned calcite crystals, (4) growth of coated grains, (5) growth of calcite rafts, and (6) dissolution of calcite and aragonite. The facies that formed during this phase can be divided into Group A, that includes the friable limestones from the interior of the tower and Group B, that forms the hard, well-lithified limestones that cap the tower around the main vent and the accessory side vents. The friable limestones of Group A are formed largely of crystal bushes whereas the hard limestones of Group B include the Fe-rich limestones and pool deposits that that are formed of various combinations of zoned calcite crystals, coated grains, and calcite rafts that are cemented by calcite.

5.1.1. Crystal bushes

Individual three-dimensional crystal bushes grew from a nucleus and expanded upwards into a bush-like structure with numerous delicate branches (Fig. 4). The bushes are typically < 2 cm high and < 1 cm in diameter but some are up to 5 cm high. Individual branches are rarely more than 1 mm in diameter (Figs. 4, 5). Although each branch is formed largely of calcite crystals, most include aragonite fans (Fig. 4B-E). There is no readily identifiable pattern to the distribution of the calcite and aragonite. Analysis of crystal bushes was difficult because (1) their delicate nature made it difficult to produce good thin sections, (2) it was largely impossible to obtain cross-sections through the branches for SEM analysis because the samples tended to fracture around rather than through the branches, (3) the cores of most branches have been partly dissolved (Fig. 5D-H), and (4) the surfaces of the branches are typically covered and disguised by Phase III precipitates that include needle-fiber calcite and calcified cyanobacteria. Thus,

information on the structure of the constituent branches had to be gleaned from those thin sections with largely intact crystal bushes (Fig. 4A, B), and fortuitous cross-sectional fractures of the branches that were evident in some SEM samples (Fig. 5F).

The aragonite fans, up to 2 mm wide and high, are characterized by needle-like crystals that radiate from a nucleus (Fig. 4C-E). In some branches, neighboring fans merged laterally to form larger, more complex arrays. Fine, concentric growth banding is a common feature of all fans. Under plane polarized light the aragonite ranges from white to dark brown in color (Fig. 4C-E).

The exact morphology of the calcite crystals could not be accurately established because of alteration and/or younger overgrowths. Thin section analysis suggests that the constituent spar crystals are typically no more than 0.5 mm high and wide and lack any consistent shape (Fig. 4C-D). Fortuitous cross-sections through some of the branches, evident on the SEM, show that many of these crystals have been extensively etched so that they are now only represented by irregular and complex skeletons formed of calcite spindles (Fig. 5D-F). In most cases the exteriors of these crystals were not affected by leaching and their exterior surfaces remained intact. In some, the branches are almost hollow (Fig. 5G, H).

Some branches are formed solely of calcite whereas others are formed of calcite and aragonite (Figs. 4A, 5A). The calcite branches are formed of numerous calcite crystals that are stacked one on top of the other. For branches formed of aragonite and calcite, the distribution of the two polymorphs is inconsistent. Thus, aragonite fans are rooted on calcite crystals and overlain by calcite crystals (Fig. 4C-E). In some cases, neighbouring branches have aragonite fans developed at a common level, but this is not always the case.

Irregular lateral connections between the vertical branches are common (Fig. 5A-C). There is no pattern to their distribution and the lateral connections seem to be formed of the same types

of crystals as the vertical branches (Fig. 5A, B). There is no identifiable branching pattern in the crystal bushes with new branches arising at irregular intervals (Fig. 4, 5).

5.1.2. Fe-rich precipitates

Many of the precipitates in the lower and central parts of ST1 are characterized by their yellowish-orange color (Fig. 3C), whereas those around the vents in the upper part of the towers are typically red to dark red in colour. Samples from the upper part of ST1 are characterized by red laminae or alternating red to orange, Fe-rich laminae and white calcite laminae (Fig. 6A). The Fe is located in delicate Fe-dendrites, up to 0.5 mm high and ~ 0.25 mm in diameter, that are characterized by complex bush-like branching patterns (Fig. 6B-C). Given that these structures are evident in thin sections throughout the calcite crystals, it appears that the Fe-dendrites developed and grew in tandem with the enveloping calcite crystals (Fig. 6C).

The colour of individual laminae appears to be linked to the density of the Fe-dendrites with the lighter coloured laminae containing fewer and more widely spaced dendrites than the darker coloured laminae, where there are densely crowded Fe-dendrites (Fig. 6A). In many laminae the Fe-dendrites have merged together.

SEM analyses show that Fe-rich precipitates are present as (1) arrays of needle-shaped crystals, typically < 1 μm long, that are organized in small clusters or radiating from a round but hollow nucleus (Fig. 7A), (2) small hollows spheres with walls formed of anhedral, Fe-rich crystals that are < 250 nm long (Fig. 7B), and (3) hollow, smooth-walled Fe-rich bodies that are up to 100 μm in diameter (Fig. 7C). Besides Fe, some of these crystals/structures also contain minor amounts of Si (Fig. 8).

The Fe-dendrites in the Shiqiang are morphologically akin to the microproblematicum *Frutexites* Maslov that have been described from Jurassic shallow marine sediments of southern

Germany and Austria (Böhm and Brachert, 1993), Pleistocene and Miocene travertines of southern Germany (Koban and Schweigert, 1993), and Devonian strata from Morocco (Jakubowicz et al., 2014). The origin of these distinctive structures is open to debate, with suggested origins ranging from organic processes, biomineralized structures, or inorganic mineralization (Böhm and Brachert, 1993). Morphologically, the Fe-dendrites are also similar to ferrihydrite precipitates found in various Japanese spring deposits that have been attributed to microbial activity (Takashima et al., 2008, 2011). No clearly defined microbes or EPS was found in the Fe-rich deposits at Shiqiang.

5.1.3. Zoned calcite crystals

Some samples from ST1 and ST2 are characterized by zoned, euhedral calcite crystals that are up to 0.50 mm long (Fig. 9). Zoning is highlighted by Fe-rich zones that alternate with Fe-poor zones (Fig. 9). These crystals include up to six clearly defined zones (Fig. 9B).

Many of the zoned calcite crystals are characterized by selective dissolution whereby some zones that were presumably formed of more soluble precipitates have been removed by dissolution (Fig. 9C, 10). Such dissolution emphasizes the zoning in the crystals (Fig. 10A, B).

5.1.4. Coated grains

Coated grains were found in small spring pools around the top vent, the side vents, and scattered throughout the precipitates in the interior of the tower (Fig. 11). Although up to 5 mm in diameter, most are < 2 mm in diameter. Irrespective of their size, distinct nuclei are absent (Fig. 11). Internally, these grains are formed of various combinations of aragonite and Fe-rich laminae. Some coated grains are formed largely of aragonite and only their outer layers are formed of Fe-rich calcite (Fig. 11A-C) whereas others are formed of numerous alternating Fe-rich and Fe-poor laminae (Fig. 11D, F). The rarest coated grains are those formed almost

entirely of Fe-rich laminae (Fig. 11E, H-I). The coated grains are typically cemented by spar calcite (Fig. 11).

5.1.4. Calcite rafts

Some deposits around the main vent of ST1 contain calcite rafts that are up to 3 mm long and 0.5 mm thick (Fig. 12). Each raft has a core formed of dense, dark-colored micrite with some having a very thin central zone that is defined by its darker color (Fig. 12). Some rafts have crystals growing from their lower surface whereas others have crystals growing from their lower and upper surfaces (Fig. 12A). That they are rafts is clearly demonstrated by the fact that at the ends of the rafts, calcite crystals radiate outwards in an orderly manner (Fig. 12C)

The rafts are either stacked one on top of another with pores between (Fig. 12A) or held in spar calcite cement (Fig. 12B).

5.2. Phase II

These white precipitates, found in the pores and cavities that exist in Phase I precipitates, contrast sharply with the earlier formed varicolored precipitates (Fig. 3C, D). The Phase II cements are formed of aragonite (Fig. 13) that locally grade into strontianite (Figs. 14-16), Mg-Si reticulate coatings (Figs. 18, 19), and calcite (Fig. 20).

5.2.1. Aragonite and associated cements

Many cavities in the Phase I precipitates are partly or completely filled with cements formed of aragonite and strontianite (Figs. 13-16). Thin section and SEM imaging shows that the aragonite cement is formed of euhedral crystals, up 2 cm long and 10 μm wide (typically ~ 5 μm), that are arranged in fans (Figs. 13, 14A-D). All of the crystals grew from a single nucleation point and progressively widened as their length increased (Fig. 14A, B). Most

crystals appear to have a hexagonal cross-section shape. Laterally linked domes (Fig. 13C-H) are internally characterized by (1) numerous closely defined growth lines, (Fig. 13C, D), (2) internal zones that are defined by color differences when viewed with plane polarized light (Fig. 13F-G), and (3) sweeping extinction patterns (Fig. 13E, H).

Some aragonite fans include thin (< 10 μm) layers formed of fibrous crystals that are < 0.25 μm wide (Fig. 14E, F). EDX analyses show that the aragonite crystals are formed of Ca (locally with a trace amount of Mg) whereas the fibrous crystals contain Ca, Sr, and Ba (Fig. 14E, 15). The Sr-rich zones, commonly < 1 μm thick, are clearly highlighted on the BSE images (Fig. 16B, E-H). The Sr-rich crystals are probably strontianite, which commonly contains up to 25% Ca and up to 4% Ba (cf., Speer and Hensley-Dunn, 1976; Radha and Navrotsky, 2013). Attempts to identify strontianite through XRD analyses failed, probably because it is only present in minor amounts.

5.2.2. Mg-Si reticulate coating

The walls of some cavities and the surfaces of some of the aragonite domes are covered with a reticulate coating (terminology following Jones and Renaut, 1996b; Jones and Peng, 2014d) formed of small, curvilinear plates that are at 90° to the substrate and intersect with each other in an irregular fashion (Fig. 18A-F). Locally, the cells between the intersecting plates, which are irregular in size and shape (Fig. 18A-C), are partly filled by calcite (Fig. 18B). Some substrates are coated with multiple generations of reticulate coatings (Fig. 18D-F) with each generation being defined by plates of different sizes (Fig. 18E). The reticulate coatings are typically extensive and cover large areas of the substrate. Locally, however, the reticulate coatings form small (< 200 μm long) ovoid masses that are formed of plates that grew outwards from a single nucleation point (Fig. 18G-I).

Numerous EDX analyses of the reticulate coatings show they are formed largely of Ca, Mg, and Si (Fig. 19). The Ca detected in many of these analyses (Fig. 19A, F, G) may, however, be coming from the underlying substrate and/or calcite cement in the cells rather than the coating itself. This suggestion is supported by the fact that the Ca content, as judged by peak height, is highly variable from spot to spot (Fig. 19).

The Mg-Si reticulate coating is morphologically and compositionally akin to similar coatings that have been documented from China (Jones and Peng, 2014d), Kenya (Casanova and Renaut, 1987; Jones and Renaut, 1996a, 1996b), and New Zealand (Jones et al., 2003).

5.2.3. Calcite cement

Many cavities in the spring deposits contain calcite cement, commonly in association with the aragonite cements (Fig. 13D, E). The calcite cement includes (1) spar crystals (Fig. 13D, E), (2) columnar crystals (Fig. 20A-D), and (3) unattached euhedral pseudo-dodecahedral crystals (Fig. 20E, F).

Irregular-shaped crystals, up to 0.5 mm long, forms isopachous coatings on cavity walls (Fig. 13A) or partly fills some of the cavities (Fig. 13D). Textural relationships indicate that precipitation of the spar calcite postdated precipitation of the aragonite cements (Fig. 13D, E).

Some substrates are covered with a calcite layer that is formed of tightly interlocking, nested crystals that are up to 60 µm long and 5 µm wide, that splayed outwards as they grew from the substrate (Fig. 20A-D). Many of these crystals have a trigonal motif (Fig. 20B).

The last formed crystals, which commonly rest on the surfaces of the earlier formed cements, are dodecahedral crystals that have beveled crystal edges (Fig. 20E, F). These crystals, < 5 µm long, commonly occur in small clusters that are not attached to a substrate (Fig. 20E, F).

5.3. Phase III

This phase, which encompasses all of the processes that postdated Phases I and II, includes (1) needle-fiber calcite crystals, (2) non-calcified and calcified filamentous microbes, and (3) microbial borings. Where present, these precipitates and microbes completely mask the older substrates.

5.3.1. Needle-fiber calcite

Many cavity walls are coated by mats formed of are morphologically complex needle-fiber calcite crystals that are up to 100 μm long but < 0.5 μm wide (Fig. 21). These mats indiscriminately covered all types of substrate (Fig. 21A). In some samples, calcified and non-calcified filamentous microbes are entwined with the needle-fiber crystals and non-calcified insects are present locally. A detailed description of these crystals was provided by Jones and Peng (2014a).

5.3.2. Non-calcified and calcified micro-organisms

Non-calcified micro-organisms include various types of filamentous microbes, calcified microbes, diatoms, euglypharids, and various types of insects are locally common, but not present in every sample that was examined (Fig. 22A-F).

The filamentous microbes, which appear fresh with no evidence of calcification or desiccation (Fig. 22A-C), are commonly enmeshed around the needle-fiber calcite crystals, suggesting that they are of similar age.

Diatoms are locally common, typically being found in small clusters (Fig. 22D). Their siliceous frustules are generally well-preserved with no evidence of abrasion or breakage. Some samples from ST3 contained numerous euglypharids that are well-preserved with their external calcareous plates, mouth, other structures being clearly evident (Fig. 22E). Fragmentary and

whole insects, present in some cavities (Fig. 22F), commonly have non-calcified filamentous microbes wrapped around them. None of the insects appeared to be calcified.

Calcified filamentous microbes are present in some samples but absent from most. This diverse array of microbes includes calcified *Syctonema julianum* (Fig. 22G, H) that are covered with amorphous calcium carbonate, acicular crystals, triradiate calcite crystals, dendrite crystals, and skeletal rhombic crystals (Jones and Peng, 2014c, their Figs. 7-11). Less common are calcified filaments, up to 25 μm long and 400 nm in diameter, with calcification characterized by a mesh-like structure with diamond-shaped apertures (Fig. 22I). These filaments are akin to reticulate filaments documented by Jones (1991, his Figs. 6B, 9E; 2011, his Fig. 5), Melim et al. (2008, their Figs. 4, 6), and Miller et al. (2012, their Figs. 2A, 2B, 4A). Other calcified filaments are covered with very finely crystalline calcite (Fig. 22J, K).

Some calcite crystals that formed early in the developmental history of the spring towers have been penetrated by borings that are up to 250 μm long and 5 μm in diameter (Fig. 22L-N). Although most borings are empty, there are rare examples that contain remnants of the formative microbe (Fig. 22N).

5.4. Diagenetic alteration

Diagenetic alteration of Phases I, II, and III precipitates includes alteration of the aragonite (Figs. 23A, B, 24A-J) and calcite (Fig. 23C-E). Dissolution mostly affected the Phase I calcite and aragonite whereas partial alteration of aragonite is mostly evident in the Phase II aragonite.

5.4.1. Aragonite alteration

Some of the Phase I aragonite that is an integral part of the crystal bushes has undergone little or no alteration (Fig. 4), whereas other aragonite has undergone extensive dissolution (Fig. 23A, B). Where evident, the cores of the aragonite fans have commonly undergone more

dissolution than the outer parts of the fans (Fig. 23A, B). In some examples, dissolution has also preferentially penetrated along certain growth zones. The degree and pattern of dissolution varies from fan to fan. In the most extreme cases, only the outer shell of the original fan remains.

Phase II aragonite is typically characterized by botryoidal masses formed of radiating crystals that have hexagonal cross-sections, well defined crystal faces and edges, and in many cases zig-zag suture lines along the length of the crystal faces that are indicative of cyclic twinning (Fig. 14A-D). Radiating clusters of crystals are evident throughout the samples (Figs. 13G, H, 14A, 24B, C, F, H). In some samples, however, these masses are no longer formed of pristine aragonite crystals. Instead, they are formed of amalgamations of small, irregular-shaped grains that are commonly < 1 μm long (Fig. 24D, E, G, I-L). The variable packing of these grains means that the microporosity varies on a microscale (Fig. 24E). In these cases, there is no direct evidence of the original aragonite crystals other than the traces of the crystals when viewed at low magnification. EDX analyses show that the small grains are formed largely of Ca. It is impossible, however, to determine if these grains are formed of calcite or if they are remnants of the original aragonite crystal. The degradation of the aragonite crystals in these arrays may be responsible for some of the darker colored zones that are apparent in thin section (Fig. 4C, E).

Throughout the samples there are rare examples of aragonite crystals that are embedded in calcite (Fig. 24K, L). In these examples, the aragonite crystals are well preserved and show no evidence of dissolution or any other type of alteration. There are no textural indications that the calcite originated from the aragonite.

5.4.2. Calcite alteration

Many calcite crystals in the branches of the crystal bushes have been dissolved to various degrees (Fig. 5D-H, 9C, 10, 23C-E). In some cases, dissolution attacked specific zones in the calcite crystals (Figs. 9C, 10) whereas in other crystals the cores were preferentially dissolved and hollow crystals resulted (Fig. 23C-E).

There is no systematic pattern to the dissolution. Thus, some branches in the crystal bushes exhibit dissolution of both the aragonite and calcite crystals, whereas other branches show evidence of aragonite dissolution but not calcite dissolution (or vice versa). Similarly within a single branch, some calcite crystals show evidence of dissolution whereas others appear unaffected.

5.5. Stable isotopes

The components that form the precipitates in the spring towers are intercalated on such a fine scale that it is impossible to segregated them and obtain the stable isotope signature of each precipitate. Thus, 26 small samples (each ~ 1 g) were extracted from the Phase I (orange-brown) and Phase II (white) precipitates so that their isotopes could be compared. XRD analyses showed that each sample is formed largely of calcite with minor amounts of quartz being present in some of them. Aragonite was detected in only 3 samples (5-10%). There is no obvious correlation between the stable isotope values and the presence/absence of aragonite.

A cross-plot of $\delta^{18}O_{calcite(SMOW)}$ versus $\delta^{13}C_{calcite(PDB)}$ shows that the samples from ST1, ST2, and ST3 can be divided into Groups A and B with the difference being largely in the $\delta^{13}C_{PDB}$ values (Fig. 25). Group A, with $\delta^{13}C_{CaCO_3(PDB)}$ values between +5.1 and +6.9‰ (average 5.9‰), are all friable samples that came from the interior of ST1 (Fig. 2A). Samples in Group B, which came from ST1, ST2, and ST3 with $\delta^{13}C_{CaCO_3(PDB)}$ values of +1.4 to +3.6‰ (average 2.6‰), are

harder and better lithified than those in Group A (Fig. 25). Group B samples from ST1 came from the uppermost part of the tower where the rocks around the main vent are well-lithified and contrast sharply with the friable rocks that form the interior of the tower.

The $\delta^{18}O_{calcite(SMOW)}$ and $\delta^{13}C_{calcite(PDB)}$ values for the samples in group B are higher than those derived from modern precipitates around springs S1 and S2, which are still active today (Fig. 25).

6. Interpretation of stable isotopes

6.1. Comparison with other Chinese hot springs

Other calcite and/or aragonite spring deposits in Yunnan Province include those at Shuzhishi (Jones and Peng, 2012), Gongxiaoshe and Zhuyuan in the Ruidian area (Jones and Peng, 2014d), Jifei (Jones and Peng, 2014b), Eryuan (Peng and Jones, 2013), and the modern springs at Shiqiang (Jones and Peng, 2016). Given that most of these samples came from or very close to the spring vent pool, they represent precipitation from spring waters that had experienced little or no downslope modifications due to processes such as degassing or evaporation. Jifei, however, is the exception because those precipitates formed on a cliff face just below a spring vent, and some downslope degassing and/or evaporation probably took place before the waters reached the site of precipitation.

From an isotopic perspective, the precipitates in the spring towers at Shiqiang contrast with the calcite-aragonite found in the other springs in two important respects.

- Group A samples have higher $\delta^{13}C_{CaCO_3(PDB)}$ values than those from the other springs (Fig. 26). Calcite dendrites from Shuzhishi, for example, have $\delta^{13}C_{CaCO_3(PDB)}$ values of -2.5 to -3.2‰, whereas the precipitates in Group A yielded values of +5.1 to +6.9‰ (Fig. 26). The

$\delta^{18}O_{CaCO_3(SMOW)}$ values of Group A, from +15.7 to +19.7‰ are generally higher than those from the other springs such as those at Jifei, which are between +9 and +13‰ (Fig. 26). The samples in Group A, however, plot along the same trend line as samples from the other springs (Fig. 26).

- Group B samples have lower $\delta^{13}C_{CaCO_3(PDB)}$ values than those in Group A, and do not plot along the $\delta^{13}C_{CaCO_3(PDB)}$ versus $\delta^{18}O_{CaCO_3(SMOW)}$ trend line that links all of the other springs and the Shiqiang Group A precipitates (Fig. 26). This is due largely to the fact that the $\delta^{18}O_{CaCO_3(SMOW)}$ values are higher than the $\delta^{18}O_{CaCO_3(SMOW)}$ values for the deposits from the other springs (Fig. 26).

6.2. Temperature derivation from O isotopes

Based on 17 samples, the $\delta^{18}O_{CaCO_3(SMOW)}$ values for Group A range from +15.7 to +19.7‰ (average 17.8‰) whereas those in Group B (9 samples) range from +13.0 to +22.0‰ (average 17.6‰). Providing (1) the $\delta^{18}O_{water(SMOW)}$ of the parent water is known, and (2) precipitation of the calcite/aragonite was in isotopic equilibrium with the parent water, the equations developed by O'Neil et al. (1969), Anderson and Arthur (1983), Hays and Grossman (1991), Kim and O'Neil (1997), and Chacko and Deines (2008) allow calculation of the original water temperature. For ease of reference, calculated temperatures derived from these equations are collectively referred to CT-I. Equations developed by Coplen (2007) and Kele et al. (2015) are also used because they argued that the other equations provide underestimates of the true temperature. Calculated temperatures from these two equations are referred to as CT-II.

Given that spring water is no longer flowing from any of the spring towers at Shiqiang, the isotopic value of the parent water is unknown. Herein, a $\delta^{18}O_{water(SMOW)}$ value of -11‰ is used

because this is the value that Jones and Peng (2016) obtained for water from the two modern, active springs that are located < 50 m from ST1 (Fig. 1C). For each sample, the CT-I values vary by up to 5°C with the equation from O'Neil et al. (1969) always giving the highest value and the equation from Kim and O'Neil (1997) always giving the lowest value (Fig. 27). All equations were applied under the assumption that a sample is formed of 100% calcite. Although true for most samples, some do contain minor amounts of aragonite. Thus, two temperatures were calculated using the Chacko and Deines (2008) method, the first assuming 100% calcite and the second assuming 100% aragonite (Fig. 27). This produced a temperature range of ~ 7°C (Fig. 27) for each sample, which spans the temperatures derived from the equations of O'Neil et al. (1969), Anderson and Arthur (1983), Hays and Grossman (1991), and Kim and O'Neil (1997).

The CT-II values are typically 8-10°C higher than the CT-I values, with the CT from the Kele et al. (2015) always being higher than that derived from the Coplen (2007) equation (Fig. 27). The CT-II values are also significantly higher than either the CT values derived for calcite or aragonite using the Chacko and Deines (2008) equation (Fig. 27).

Overall, the samples yielded CT-I values of 12° to 52°C, whereas the CT-II values range from 21 to 61°C (Fig. 27). Samples in Group A yielded CT-I values of 13 to 34°C, with most being in the 20 to 30°C range, whereas the CT-II values range from 21 to 44°C with most in the 30 to 40°C range (Fig. 27). For Group B, the CT-I values ranged from 10 to 50°C whereas the CT-II values ranged from 20 to 61°C (Fig. 27). Irrespective of the equation used, Group B can be divided into B1 and B2, wherein samples in B2 yielded higher CT than those in B1 (Fig. 27).

Irrespective of the equation used, the CT derived from the calcite and aragonite that are presently forming in and close to the active vent pools S1 and S2 at Shiqiang are not in

agreement with the measured water temperatures (Jones and Peng, 2016). The same is true for other calcite and aragonite precipitates at other hot springs in Yunnan Province, including those at Gongxiaoshe, Zhuyuan, Jifei, and Eryuan. Such discrepancies between the CT and measured water temperatures (MT) are due to either (1) the precipitates not being in isotopic equilibrium with the spring water, or (2) the precipitates formed from older spring waters with an isotopic signature that was different from that of the modern spring water.

6.2. Interpretation of C isotopes

$\delta^{13}C$ values derived from carbonate deposits in spring systems have been used to divide them into meteogene and thermogene travertines (e.g., Pentecost and Viles, 1994; Pentecost, 1995, 2005; Kele et al., 2003). Although based on the $\delta^{13}C$ of the carrier CO_2, this division is also characterized by contrasts in other aspects of the deposits (e.g., Kele et al., 2003, their Table 2). According to Pentecost (2005, his Fig. 46a, c) the $\delta^{13}C_{CaCO_3}$ of the thermogene travertines range from –3 to +8‰ (average +3.89‰), whereas the $\delta^{13}C_{CaCO_3}$ of the meteogene travertine ranges from 0 to –11‰ (average –7‰). Under this scheme, the precipitates from Shiqiang, with $\delta^{13}C_{CaCO_3(PDB)}$ values of +5.1 to +6.9‰ (average +5.9‰) for Group A and $\delta^{13}C_{CaCO_3(PDB)}$ values of +1.4 to +3.6‰ (average +2.6‰) for Group B belong to the thermogene class. Other aspects of the Shiqiang deposits are also consistent with other features of thermogene travertines as outlined by Pentecost and Viles (1994), Pentecost (1995) and Kele et al. (2003, their Table 2).

In situations where spring activity has ceased, the $\delta^{13}C_{CO_2\,(PDB)}$ of the carrier CO_2 can be derived from the $\delta^{13}C_{CaCO_3(PDB)}$, as suggested by Panichi and Tongiorgi (1976). This is important because it can provide clues as to the origin of the CO_2 and hence, the circulation patterns of the spring water. Kele et al. (2011), however, argued that the $\delta^{13}C_{CO_2\,(PDB)}$ value must

be derived from precipitates close to the spring vent pool so that the isotopes do not reflect downslope modification of the spring waters by degassing and/or evaporation. Panichi and Tongiorgi (1976) related the $\delta^{13}C_{CO_2}$ and $\delta^{13}C_{CaCO_3}$ by the equation (1).

$$\delta^{13}C_{CO_2} = 1.2(\delta^{13}C_{CaCO_3}) - 10.5 \quad (1)$$

This equation was subsequently used by Minissale et al. (2002) in their analysis of Quaternary travertines from central Italy and Kele et al. (2003, 2011) in their studies of various Hungarian and Turkish travertines. The equation proposed by Panichi and Tongiorgi (1976), however, ignores the fact that C fractionation is temperature dependent as shown by Bottinga (1968), Emrich et al. (1970), Romanek et al. (1992), Chacko et al. (2001), and Chacko and Deines (2008). Although calculated, values obtained from the Panichi and Tongiorgi (1976) equation were not used because it does not account for the T dependency of C fractionation.

For samples from the spring towers at Shiqiang, the $\delta^{13}C_{CO_2}$ was calculated for water temperatures of 25°C and 40°C because (1) it includes most of the CT derived from $\delta^{18}O_{CaCO_3}$, and (2) it matches the range of temperature values covered by some of experimental work used to derived the T dependency of the C fractionation factor (e.g., Romanek et al., 1992). The equation (2) derived by Romanek et al (1992) was on experiments over a temperature range of 20 to 40°C.

$$\delta^{13}C_{CO_2} = \delta^{13}C_{CaCO_3} - ((11.98 - (0.12*T)) \quad (2)$$

where: T = temperature in Celsius

The values obtain using this equation are not used herein because the calculated $\delta^{13}C_{CO_2}$ values at 40°C are significantly lower than those obtained from the other equations (Fig. 28).

Equation (3) is derived from curve 'b' of Figure 1 in Emrich et al. (1970).

$$\{(1000 + \delta^{13}C_{CaCO3}) / EXP[-7.762x10^{-3} + 5.244 \times 10^{-3}(1000/T)]\} - 1000 \quad (3)$$

where: T = temperature in Kelvin

Equation (4), which comes from Chacko et al. (2001, Appendix 3, p. 76), is based on data in Chacko et al. (1991).

$$\delta^{13}C_{CO2} = \{(1000 + \delta^{13}C_{CaCO3}) * EXP[(-0.10028 + 5.4173x - 2.5076x^2 + 0.47193x^3 - 0.049501x^4 + 0.0027046x^5 - 0.000059409x^6)/1000]\} - 1000 \quad (4)$$

where: $x = 10^6/T^2$ and T = temperature in Kelvin

The values obtained from equation (3) Emrich et al. (1970) and equation (4) of Chacko et al. (2001) are close when a T of 25°C is used, and essentially identical when a T of 40°C is used (Fig. 28).

Herein, the values obtained from the Chacko et al. (1991) equation are used because it was based on rigorous experimental and theoretical considerations. For Group A, the $\delta^{13}C_{CO_2\,(PDB)}$ ranges from –5.5 to –3.7‰ (average –4.6‰: = A(25)) if T is 25°C and from –8.9 to –2.1‰ (average –3.7‰: = A(40)) if a T of 40°C is used (Fig. 28). For Group B, the calculated $\delta^{13}C_{CO_2\,(PDB)}$ ranges from –7.0 to –9.1‰ (average –7.8‰: = B(25)) if a T is 25°C and from –5.4 to –7.6‰ (average –6.3‰: = B(40)) if a T of 40°C is used (Fig. 28). At both temperatures, the contrast in the $\delta^{13}C_{CO_2(PDB)}$ of Groups A and B is readily apparent (Fig. 28).

6.3. Integration of O and C isotope interpretations

Interpretations based on the stable isotopes suggest that the precipitates in Group A formed from thermogene water that had CT of 20–35°C, and possibly as high as 41°C (Fig. 27). The stable isotopes for these friable limestones, which form the interior parts of the spring towers,

also plot along the same trend line that relates the precipitates from other springs in the Yunnan Province (Fig. 26). Although the O isotopes from the harder limestones in Group B indicate precipitation from waters with similar temperatures to those in Group A, three samples yielded CT of 35 to 50°C, and possibly as high as 61°C (Fig. 27). Nevertheless, these precipitates also formed from thermogene waters that had different $\delta^{13}C_{CaCO_3}$ isotopes signatures from those in Group A (Fig. 25). The isotope values for Group B do not plot along the same trend line as defined for Group A and other spring deposits from Yunnan Province (Fig. 26).

It has been argued that thermal waters in China are largely of meteoric origin because the $\delta^{18}O$ and δD of these waters, including that from the modern springs at Shiqiang (Jones and Peng, 2016, their Fig. 14), all plot on the Global Meteoric Water Line (Zhou et al., 2009, their Fig. 2; Liu et al., 2015). For the precipitates that form the spring towers at Shiqiang, the water temperatures derived from the $\delta^{18}O$ values and the calculated $\delta^{13}C_{CO_2(PDB)}$ values clearly indicate that those meteoric waters were modified before being ejected from the spring vents. The high CT indicate heating at depth, probably as a result of deep-circulation and/or flow close to a magma chamber. The $\delta^{13}C_{CO_2(PDB)}$ values may have been developed through interaction with CO_2-rich thermal fluids, hydrolysis, decarbonisation of limestone, atmospheric CO_2, or soil CO_2 (cf., Pentecost and Viles, 1994; Kele et al., 2003; Pentecost, 2005). Based on the ranges of $\delta^{13}C_{CO_2}$ given by Sharp (2007, his Fig. 7.2), more negative values would be expected if atmospheric CO_2 or soil CO_2 had interacted with the spring water. The $\delta^{13}C_{CO_2}$ values derived from the precipitates in Groups A and B are, however, consistent with the range of CO_2 values associated with volcanic gas samples and other deep-seated processes as given by Sharp (2007, his Fig. 7.2). Irrespective of the exact cause of the $\delta^{13}C_{CO_2}$, the contrast in values derived from

the precipitates in Groups A and B indicate that subterranean conditions changed, possibly as a result of increased volcanic activity if it is accepted that volcanic CO_2 gas may have been responsible for modification of the water.

The contrast between the stable isotopes of Group A and Group B precipitates indicates that during growth and development of the towers there was a significant change in the processes that dictated precipitation. For Group A, the high $\delta^{13}C_{CaCO_3}$ values and high $\delta^{18}O_{CaCO_3}$ values, relative to other spring deposits in Yunnan (Fig. 26), suggest that rapid CO_2 degassing and evaporation may have underpinned precipitation. The lower $\delta^{13}C_{CaCO_3}$ values for the precipitates in Group B suggest that the CO_2 degassing was less important during their precipitation and that evaporation may have been more important (Fig. 26).

7. Discussion

The spring towers known from a few localities worldwide are largely inactive. Although their origin is still open to debate, Bargar (1978) suggested that the towers continue to grow until there is insufficient artesian pressure to continue lifting the water over the lip of the pool. Likewise, Dunzhujiacan and Wu (1985, their Fig. 128) noted that the "cones" will cease to grow once the spring water head is equal to its height and Scheuer and Schweitzer (1985, p. 397) argued that the height is controlled by "…the pressure conditions of the hydrodynamic regime associated with the springs." As such, these structures are self-limiting and the different heights of these structures, ranging up to 14 m (e.g., Liberty Cap, Yellowstone National Park; Bargar, 1978) is largely a reflection of the variable artesian pressures found at different locations. Being no more than 4 m high, the spring towers at Shiqiang obviously developed from waters with lower artesian pressures than those associated with the growth of towers that are up 13 m high in the Rongma area of Tibet (Gao et al., 2013, their Fig. 2), 7.1 m high in the Jifei area of China

(Liu et al., 2012, their Fig. 3), 7 m high in the Longma'er travertine ("Stone Forest") of Tibet (Dunzhujiacan and Wu, 1985, their Fig. 128), and 4.8 m in the "Travertine Totem Forest" of Yellowstone National Park (Hutchinson and Thompson, 1992). Today, most spring towers are inactive. At some localities, such as Jifei, there are isolated towers that have minor amounts of hot water emerging at their top but with no associated precipitation (Liu et al., 2012). The spring towers at Shiqiang are now inactive and there does not appear to be any historical accounts that provide any information pertaining to their history. Thus, the time when they were active is unknown. At Jifei, ~ 115 km SE of Shiqiang, Liu et al. (2015) suggested that most of the travertine formation took place 10,000 to 20,000 years ago. Similarly, Gao et al. (2013) argued the spring towers in the Rongma, Tibet formed between 11,500 and 4600 years ago, when the climate was warmer and wetter than today.

At Shiqiang, determination of the environmental conditions that existed when the spring towers were active is complicated because of the anthropogenic modifications that took place when the northwest part of the area was developed for tourism. Man-made lakes were formed when container walls and elevated pathways were constructed around most of the towers (Fig. 2A). Without that construction, the present-day lakes would not exist. The spring towers located in the farmer's field in the southeast part of the site (Fig. 1C) are on dry land and there is no direct evidence that they were ever partly or fully submerged by lake water (Fig. 2A, B). For the mushroom-shaped towers in the northwest lake, it could be argued that the base of the cap was the water level that existed when the towers were active. With this scenario, the "stem" would have formed under water (or perhaps sediment) whereas the "cap" grew above water level. Unusual mushroom-shaped speleothems in Santa Catalina Cave, Cuba, which are up to 2.5 m high and 90 cm in diameter have a distinct stipe (stem) and cap (Bontognali et al., 2016). These

complex structures, which may have been microbially mediated, reflect progressive changes in the depositional history of the cave such that (1) a stalagmite that formed while the cave was dry, (2) the stalagmite was covered by calcite rafts and a mammalated coating when the cave was submerged, and (3) the cap formed as water level oscillated up and down (Bontognali et al., 2016). The fact that the tops and bases of the caps are all at the same level supports the notion that their growth was controlled by oscillating water levels. Although the mushroom-shaped spring towers at Shiqiang are superficially similar in morphology, the bases of the "caps", as evident from two towers shown in Figures 3B and 3C, are at different levels. Thus, with the evidence currently available, it is impossible to know the significance of the base levels of the "caps" that exist on some of these towers. The spring towers exposed in the farmer's field have parallel sides and there is no evidence of mushroom shapes (Fig. 3A, B). Herein, the spring towers are considered to have developed entirely on land.

Calculated water T based on the $\delta^{18}O_{CaCO_3}$ must be treated with caution because it assumes that the precipitates formed in isotopic equilibrium with the parent waters, and that the modern spring water is a good analog for the spring waters from which the towers developed. Such caution is warranted given that the CT for precipitates around the two modern springs (S1 and S2) does not match to the MT of the modern spring water (Jones and Peng, 2016). Nevertheless, the calculated temperatures derived from the precipitates in the spring towers indicate that the parent waters associated with the towers were warm to hot, rather than cold. The $\delta^{13}C_{CO_2}$, as derived from the $\delta^{13}C_{CaCO_3}$, indicates that the spring water had a thermogene signature (as defined by Pentecost, 2005). Combined, these data indicate that the springs were fed by meteoric waters that had been heated at depth with modification of the CO_2, possibly as a result of interaction with volcanic CO_2 gases.

From a petrographic perspective, the development of ST1 at Shiqiang involved Phase I-A and I-B that resulted in construction of the tower, Phase II that involved precipitation of white cements in the cavities throughout the tower, and lastly, Phase III that involved precipitation of needle-fibre calcite and calcification of some of the microbes that invaded the tower. A recurring theme with Phases I and II is the alternation between calcite and aragonite precipitation. Establishing the conditions that lead to the precipitation of these two polymorphs in spring environments has long been the subject of considerable debate (e.g., Meigen, 1901; Suganuma, 1928; Kitano, 1962a, 1962b; Folk, 1994). Peng and Jones (2013) and Jones and Peng (2014d, 2014b), based on analyses of various spring deposits in Yunnan Province, suggested that precipitation of aragonite and calcite may be controlled by relatively minor fluctuations in saturation levels that are related to microbial activity and/or the rate of CO_2 degassing. Irrespective of the actual cause, it is difficult to ascribe the precipitation of these two polymorphs to specific large scale variables such as water T, as suggested by Folk (1994). Jones and Peng (2016) reached the same conclusion for the intimately associated aragonite and calcite associated with the two active springs (S1, S2 – Fig. 1C) at Shiqiang.

The Phase I-A friable, porous limestones that form the core of ST1 are constructed of delicate, randomly branching crystal bushes that are formed largely of aragonite and calcite (Figs. 4, 5). The delicacy of these bushes (Fig. 4A, B) raises the possibility that their growth may have been mediated by microbes and their associated biofilms. Despite extensive searching of numerous samples, no direct evidence of microbial involvement was found. Hence, a microbial origin for the towers cannot be demonstrated. Dissolution of some of the aragonite and calcite in these bushes (Figs. 5B-H, 23) offers testimony to ever changing fluids that through time mediated both precipitation and dissolution of aragonite and calcite.

The hard, low porosity limestones found around the vents at the top of ST1 and the upper parts of the tower may have formed during the waning stages of spring activity. This probably occurred when the height of the tower was approaching the maximum height of water evulsion that was controlled by the artesian pressure. Alternatively, this change may have been triggered by a decrease in the artesian pressure that caused a significant change in water flow from the spring vent. It is clear from the stable isotopes of these precipitates that the isotopic composition of the spring water had changed (Figs. 25, 26, 28), largely as a result of the ^{13}C becoming more depleted. Irrespective of the underlying cause, this change was accompanied by a Fe-enrichment of the spring water, as is evident from the reddish hues of the precipitates that formed during this phase. The fact that the coated grains and some of the calcite crystals are characterized by the alternating zones of iron-rich calcite and iron-poor calcite indicates that the Fe content of the spring water varied over short periods of time.

Conspicuous white cements, formed largely of alternating calcite and aragonite, are common throughout the friable limestones in ST1 (Figs. 3C, D, 13). Locally, the aragonite passes laterally and vertically into strontianite (Fig. 16). Although rare, strontianite has been reported from deposits in Miette Hot Springs in Canada (Bonny and Jones, 2003), spring travertines in the Songwe River valley in Tanzania (Pisarskii et al., 1998), and cave deposits in the U.S.A. (Hill and Forti, 1997), Spain (Fernández-Rubio et al., 1975), and Iran (Calaforra et al., 2013). The $SrCO_3$ – $CaCO_3$ solid solution series, which can produce an isomorphic series between aragonite and strontianite, may have up to 25 mol % Ca and 5% Ba substituted in the strontianite (Speer and Hensley-Dunn, 1976; Radha and Navrotsky, 2013), as is the case with the strontianite found in the Shiqiang deposits (Fig. 16). Strontianite precipitation takes place when the parent water has a high Sr/Ca ratio (Helz and Holland, 1965), which can be achieved by (1)

the preferential solution of celestite, (2) the preferential solution of barite, and/or (3) recrystallization of aragonite to calcite (Helz and Holland, 1965). Caloforra et al. (2013) suggested that strontianite precipitation in Serizjan Cave (Iran) required a high Sr/Ca ratio in the rising thermal waters that had, along their flow path, dissolved gypsum and celestine. By analogy, this suggests that the spring waters at Shiqiang must have periodically experienced an increase in their Sr/Ca ratio by enrichment in Sr and/or depletion in Ca. The source of the Sr is unknown because the subsurface geology of the Shiqiang area is unknown.

Mg-Si reticulate coatings are commonly associated with the calcite, aragonite, and strontianite of Phase II (Fig. 18, 19). The origin of these distinctive reticulate precipitates, also known from springs in China (Jones and Peng, 2014d), Kenya (Casanova and Renaut, 1987; Jones and Renaut, 1996b, 1996a), New Zealand (Jones et al., 2003), remains a matter of debate (Jones and Peng, 2014d). Nevertheless, they are a record of times when the spring waters carried sufficient Mg and Si to allow formation of these precipitates. Precipitation of the strontianite and the Mg-Si reticulate coatings collectively point to periods when the spring waters became enriched with Sr, Mg, and/or Si.

Phase III diagenesis, which probably developed after the springs had ceased to function, is characterized by cements and calcified microbes that coat the walls of the cavities, irrespective of the type and age of the precipitates that form them. Needle-fiber calcite cement, characterized by diverse and complex crystal forms (Jones and Peng, 2014a), forms dense mats that coat and completely mask the underlying substrates (Fig. 21). The fact that they cover all types of substrates indicates that they are one of the youngest components in the towers. This phase of activity also involved a wide variety of microbes, diatoms, and insects (Fig. 22). Indeed, microbial activity during Phase III appears to have been far greater than during Phases I and II.

Although many of the microbes show no evidence of calcification (Fig. 22B, C), others are extensively calcified (Fig. 22G-K). Examples include *Scytonema julianum* that is covered with complex, 3-dimensional dendrites (Jones and Peng, 2014c), and reticulate filaments (Fig. 22I). The fact that some of these insects and microbes are locally entwined with the needle-fibre calcite mats indicates that they all developed at the same time within the confines of the spring tower (Fig. 22C). Borings in some of the calcite crystals by filamentous microbes (Fig. 22L-N) probably formed at the same time.

8. Conclusions

Integration of field observations, detailed petrographic data, and isotopic signatures of the spring towers found at Shiqiang in Yunnan Province, China, has led to the following conclusions:

- Although the age of the spring towers is not known, they must have developed when artesian pressure, higher than it is today, resulted in spring water being ejected to many meters above ground level. This may have been related to a time period when rainfall was higher than it is today.
- The spring towers evolution involved three distinct phases: (1) Phase I (A and B) that primarily involved the construction of the tower through the precipitation of crystal bushes formed of calcite and aragonite (Phase I-A) and later, calcite that was commonly Fe-rich; (2) Phase II that led to the precipitation of cements (calcite, aragonite, strontianite, Mg-Si reticulate coatings) in pores in the Phase I precipitates, and (3) Phase III that involved the precipitation of mats of needle-fibre calcite crystals that coated all of the earlier formed substrates and was accompanied by an infestation of microbes (commonly calcified), diatoms, and insects.

- Calcite and aragonite precipitation was probably not in isotopic equilibrium with the spring water. Nevertheless, CO_2 degassing along with some evaporation of the water was probably responsible for the precipitates in Group A. By comparison, Group B precipitates seem to have developed after CO_2 degassing had decreased and evaporation had become more important.
- Temporal variations in saturation levels with respect to calcite and aragonite led to the alternation between periods of precipitation and dissolution of calcite and aragonite. At other times, aragonite was transformed to calcite.
- Temporal variations in the trace element content of the spring waters led to the precipitation of Fe-rich calcite as the amount of Fe increased, strontianite as the Sr/Ca ratio increased, and Mg-Si reticulate coatings as the Mg and Si content increased.
- Interpretation of the $\delta^{18}O$ and $\delta^{13}C$ suggests that spring water was of meteoric origin and was heated at depth with modification of its $\delta^{13}C$ signal and would, therefore, qualify as a thermogene spring according to the classification of Pentecost (2005).

Acknowledgements

This research was possible because of funding received from the Natural Sciences and Engineering Council of Canada (Grant to Jones), the National Natural Science Foundation of China (grants 41172309 and 41272370 to Peng), the Frontier Project of the Chinese Academy of Science (SIDSSE1301 to Peng), and the Strategic Priority Research Program of the Chinese Academy of Sciences (XDB06020000 to Peng). We are indebted to all these organizations for the support of this work. We are greatly indebted to Dr. T. Chacko who provided advice regarding the stable isotopes and derived some of the equations used for the derivation of C

isotope fractionation factors. We are also greatly indebted to Drs. E. Capezzuoli, M. Gradzinski, J. De Waele, J. Knight, and an anonymous reviewer for their critical reviews of an earlier version of this paper.

REFERENCES

Anderson, T.F., Arthur, M.A., 1983. Stable isotopes of oxygen and carbon and their application to sedimentologic and palaeoenvironmental problems. In: Arthur, M.A., Anderson, T.F., Kaplan, I.R., Veizer, J., Land, L.S. (Eds.), Stable Isotopes in Sedimentary Geology. Society of Economic Paleontologists and Mineralogists, Tulsa, Oklahoma, pp. 1.1-1.151.

Bargar, K.E., 1978. Geology and thermal history of Mammoth Hot Springs, Yellowstone National Park, Wyoming. Geological Survey Bulletin 1444, United States Department of the Interior, 1-55.

Böhm, F., Brachert, T.C., 1993. Deep-water stromatolites and *Frutexites* Maslov from the Early and Middle Jurassic of S. Germany and Austria. Facies 28, 145-168.

Bonny, S.M., Jones, B., 2003. Microbes and mineral precipitation, Miette Hot Springs, Jasper National Park, Alberta, Canada. Canadian Journal of Earth Sciences 40, 1483-1500.

Bontognali, T.R.R., D'Ageli, I.M., Tisato, N., Vasconcelos, C., Bernasconi, S.M., Gonzales, E.R.G., De Waele, J., 2016. Mushroom speleothems: Stromatolites that formed in the absence of phototrophs. Frontiers in Earth Science 4, 1-8.

Bottinga, Y., 1968. Calculations of fractionation factors for carbon and oxygen isotopic exchange in the system calcite-carbon dioxide-water. Journal of Physical Chemistry 72, 800-808.

Calaforra, J.M., de Waele, J., Forti, P., Galli, E., Edbadi, M., 2013. Strontianite from Serizjan Cave (Iran): A new occurrence of this rare cave mineral with a discussion of its genesis. International Congress of Speleology Proceedings, pp. 449-452.

Casanova, J., Renaut, R.W. (Eds.), 1987. Les stromatolites du milieu hydrothermal. Le demi-graben de Baringo-Bopgoria, Rift Gregory, Kenya: 30,000 ans d'histoire hydrologique et

sédimentaire, Bulletin 11. Centres de Recherches Exploration - Production Elf - Aquitaine, 484-490 pp.

Chacko, T., Deines, P., 2008. Theoretical calculation of oxygen isotope fractionation factors in carbonate systems. Geochimica et Cosmochimica Acta 72, 3642-3660.

Chacko, T., Cole, D.R., Horita, J., 2001. Equilibrium oxygen, hydrogen and carbon isotope fractionation factors applicable to geological systems. In: Valley, J.W., Cole, D.R. (Eds.), Reviews in Mineralogy and Geochemistry, Mineralogical Society of America, Virginia, USA, pp. 1-81.

Chacko, T., Mayeda, T.K., Clayton, R.N., Golsmith, J.R., 1991. Oxygen and carbon isotope fractionation between CO_2 and calcite. Geochimica et Cosmochimica Acta 55, 2867-2882.Chafetz, H.S., Guidry, S.A., 2003. Deposition and diagenesis of Mammoth Hot Springs travertine, Yellowstone National Park, Wyoming, U.S.A. Canadian Journal of Earth Sciences 40, 1515-1529.

Coplen, T.B., 2007. Calibration of the calcite-water oxygen-isotope geothermometer at Devils Hole, Nevada, a natural laboratiry. Geochimica et Cosmochimica Acta 71, 3948-3957.

Du, J., Liu, C., Fu, B., Ninomia, Y., Zhang, Y., Wang, C., Wang, H., Sun, Z., 2005. Variations of geothermometry and chemical-isotope compositions of hot spring fluids in the Rehai geothermal field, southwestern China. Journal of Volcanology and Geothermal Research 142, 243-261.

Dunzhujiacan, Wu, F., 1985. A Pearl on the Roof of the World: The Yanbajain Geothermal Demonstration Power Plant. China Pictorial Publishing Company, Beijing, 152 pp.

Emrich, K., Ehhalt, D.H., Vogel, J.C., 1970. Carbon isotope fractionation during the precipitation of calcium carbonate. Earth and Planetary Science Letters 8, 363-371.

Fernández-Rubio, R., Eraso, A., Ortega, M., Arana, R., Rojas, E., 1975. Estudio de la sima termal de las fumarolas (Montevives, Granada, España). Annales de Spéléologie 30, 287-302.

Folk, R.L., 1994. Interaction between bacteria, nannobacteria, and mineral precipitation in hot springs of central Italy. Geographie physique et Quaternaire 48, 233-246.

Gao, J., Zhou, X., Fang, B., Li, T., Tang, L., 2013. U-series dating of the travertine depositing near Rongma hot springs in northern Tibet, China, and its paleoclimatic implication. Quaternary International 298, 98-106.

Guo, X., Chafetz, H.S., 2012. Large tufa mounds, Searles Lake, California. Sedimentology 59, 1509-1535.

Hayden, F.V., 1872. Preliminary report of the United States Geological Survey of Montana and portions of adjacent territories: Being a fifth annual report of progress [for the year 1971]. Washington, D.C., Department of the Interior, 537 p.

Hays, P.D., Grossman, E.L., 1991. Oxygen isotopes in meteroic calcite cements as indicators of continental palaeoclimate. Geology 19, 441-444.

Helz, G.R., Holland, H.D., 1965. The solubility and geologic occrrence of strontianite. Geochimica et Cosmochimica Acta 29, 1303-1315.

Hill, C.A., Forti, P., 1997. Cave Minerals of the World. National Speleological Society, Alabama, U.S.A., 463 pp.

Houssein, B., 2010. Geochemistry overview of hot springs from the Lake Abhe area: Republic of Djibouti. Third East African Rift Geothermal Conference, pp. 158-169.

Houssein, B., Chandrasekharam, D., Chandrasekhar, V., Jalludin, M., 2013. Geochemistry of thermal springs around Lake Abhe, Western Djibouti. International Journal of Sustainable Energy 33, 1-13.

Hutchinson, R.A., Thompson, J.M., 1992. The Travertine Totem Forest of Yellowstone National Park, USA – geologic controls and geochemistry. In: Kharaka, Y.K., Maest, A.S. (Eds.), 7th International Symposium on Water-Rock Interaction. International Association of Geochemists and Cosmochemists, Park City, Utah, U.S.A., pp. 1419-1421.

Jettestuen, E., Jamtveit, B., Podladchikov, Y.Y., deVilliers, S., Amunsden, H.E.F., Meakin, P., 2006. Growth and characterization of complex mineral surfaces. Earth and Planetary Science Letters 249, 108-118.

Jones, B., 1991. Genesis of terrestrial oncoids, Cayman Islands, British West Indies. Canadian Journal of Earth Sciences 28, 382-397.

Jones, B., 2011. Biogenicity of terrestrial oncoids formed in soil pockets, Cayman Brac, British West Indies. Sedimentary Geology 236, 95-108.

Jones, B., Peng, X., 2012. Intrinsic versus extrinsic controls on the development of calcite dendrite bushes, Shuzhishi Spring, Rehai geothermal area, Tengchong, Yunnan Province, China. Sedimentary Geology 249-250, 45-62.

Jones, B., Peng, X., 2014a. Abiogenic growth of needle-fiber calcite in spring towers at Shiqiang, Yunnan Province, China. Journal of Sedimentary Research 84, 1021-1040.

Jones, B., Peng, X., 2014b. Hot spring deposits on a cliff face: A case study from Jifei, Yunnan Province, China. Sedimentary Geology 302, 1-28.

Jones, B., Peng, X., 2014c. Multiphase calcification associated with the atmophytic cyanobacterium *Scytonema julianum*. Sedimentary Geology 313, 91-104.

Jones, B., Peng, X., 2014d. Signatures of biologically influenced $CaCO_3$ and Mg-Fe silicate precipitation in hot springs: Case study from the Ruidian geothermal area, Western Yunnan Province, China. Sedimentology 61, 56-89.

Jones, B., Peng, X., 2016. Mineralogical, crystallographic, and isotopic constraints on the precipitation of aragonite and calcite at Shiqiang and other hot springs in Yunnan Province, China Sedimentary Geology 345, 103-125.

Jones, B., Renaut, R.W., 1996a. Morphology and growth of aragonite crystals in hot-spring travertines at Lake Bogoria, Kenya Rift Valley. Sedimentology 43, 323-340.

Jones, B., Renaut, R.W., 1996b. Influence of thermophilic bacteria on calcite and silica precipitation in hot springs with water temperatures above 90°C: evidence from Kenya and New Zealand. Canadian Journal of Earth Sciences 33, 72-83.

Jones, B., Renaut, R.W., Rosen, M.R., 2003. Silicified microbes in a geyser mound: the enigma of low-temperature cyanobacteria in a high-temperature setting. Palaios 18, 87-109.

Jakubowicz, M., Belka, Z., and Berkowski, B., 2014. *Frutexites* encrustations on rugose corals (Middle Devonian, southern Morocco): Complex growth of microbial microstromatolites. Facies 60, 631-650.

Kearey, P., Wei, H., 1993. Geothermal fields of China. Journal of Volcanology and Geothermal Research 56, 415-428.

Kele, S., Breitenbach, S.F.M., Capezzuoli, E., Meckler, A.N., Ziegler, M., Millan, I.M., Kluge, T., Deák, J., Hanselmann, K., John, C.M., Yan, H., Liu, Z., Bernasconi, S.M., 2015. Temperature dependence of oxygen- and clumped isotope fractionation in carbonates: A study of travertines and tufas in the 6–95°C temperature range. Geochimica et Cosmochimica Acta 168, 172-192.

Kele, S., Özkul, M., Fórizs, I., Gökgöz, A., Baykara, M.O., Alçiçek, M.C., Németh, T., 2011. Stable isotope geochemical study of Pamukkale travertines: New evidences of low-temperature non-equilibrium calcite-water fractionation. Sedimentary Geology 238, 191-212.

Kele, S., Vaselli, O., Szabó, Minissale, A., 2003. Stable isotope geochemistry of Pleistocene travertine from Budakalász (Buda Mts, Hungary). Acta Geologica Hungarica 46, 161-175.

Kempe, S., Kazmierczak, J., Landmann, G., Konak, T., Reimer, A., Lipp, A., 1991. Largest known microbialites discovered in Lake Van, Turkey. Nature 349, 605-608.

Kim, S.-T., O'Neil, J.R., 1997. Equilibrium and nonequilibrium oxygen isotope effects in synthetic carbonates. Geochimica et Cosmochimica Acta 61, 3461-3475.

Kitano, Y., 1962a. The behavior of various inorganic ions in the separation of calcium carbonate from a bicarbonate solution. Bulletin of the Chemical Society of Japan 35, 1973-1980.

Kitano, Y., 1962b. A study of the polymorphic formation of calcium carbonate in thermal springs with an emphasis of the effect of temperature. Journal of Earth Sciences, Nagoya University 35, 1980-1985.

Koban, C.G., Schweigert, G., 1993. Microbial origin of travertine facies – two examples from southern German (Pleitocene Stuttgart travertines and Miocene Riedöschingen travertine). Facies 29, 251-264.

Li, R., Jones, B., 2014. Calcareous crusts on exposed Pleistocene limestones: A case study from Grand Cayman, British West Indies. Sedimentary Geology 299, 88-105.

Liu, Y., Zhou, X., Deng, Z., Fang, B., Tsutomu, Y., Zhao, J.X., Wang, X., 2015. Hydrochemical characteristics and genesis analysis of the Jifei hot spring in Yunnan, southwestern China. Geothermics 53, 38-45.

Liu, Y., Zhou, X., Fang, B., Zhou, H., Yamanaka, T., 2012. A preliminary analysis of the formation of travertine and travertine cones in the Jifei hot spring, Yunnan, China. Environmental Earth Sciences 66, 1887-1896.

Meakin, P., Jamtveit, B., 2010. Geological pattern formation by growth and dissolution in aqueous systems. Proceedings of the Royal Society A 466, 659-694.

Meigen, W., 1901. Eine einfache Reaktion zue unterscheidung von aragonit und kalkspath. Zentralblatt fuer Mineralogie, Geologie, und Paleontologie 1901, 577-578.

Melim, L.A., Northup, D.E., Spilde, M.N., Jones, B., Boston, P.J., Bixby, R.J., 2008. Reticulated filaments in cave pool speleothems: microbe or mineral? Journal for Cave and Karst Studies 70, 135-141.

Miller, A.Z., Hernández-Mariné, M., Jurado, V., Dionísio, A., Barquinha, P., Fortunato, E., Afonso, M.J., Chaminé, H.I., Saiz-Jimenez, C., 2012. Enigmatic reticulated filaments in subsurface granite. Environmental Microbiology Reports 4, 596-603.

Minissale, A., Kerrick, D.M., Magro, G., Murrell, M.T., Paladini, M., Rihs, S., Sturchio, N.C., Tassi, F., Vaselli, O., 2002. Geochemistry of Quaternary travertines in the region north of Rome (Italy): Structural, hydrologic and paleoclimatic implications. Earth and Planetary Science Letters 203, 709-728.

O'Neil, J., Clayton, R., Mayeda, T., 1969. Oxygen isotope fractionation in divalent metal carbonates. Journal of Chemical Physics 51, 5547-5558.

Panichi, C., Tongiorgi, E., 1976. Carbon isotopic composition of CO_2 from springs, fumaroles, mofettes and travertines of central and southern Italy: A preliminary prospection method of geothermal areas. Proceedings, 2nd U.N. Symposium on the Development and Use of Geothermal Energy, San Francisco, pp. 815-825.

Peng, X., Jones, B., 2013. Patterns of biomediated $CaCO_3$ crystal bushes in hot spring deposits. Sedimentary Geology 294, 105-117.

Pentecost, A., 1995. The Quaternary travertine deposits of Europe and Asia Minor. Quaternary Science Reviews 14, 1005-1028.

Pentecost, A., 2005. Travertine. Springer, Berlin Heidelberg, 445 pp.

Pentecost, A., Viles, H., 1994. A review and reassessment of travertine classification. Géographie physique et Quarernaire 48, 305-314.Pisarskii, B.I., Konev, A.A., Levi, K.G., Delvaux, D., 1998. Carbon dioxide-bearing alkaline hydrotherms and strontium-bearing travertines in the Songwe River valley (*Tanzania*). Russian Geology and Geophysics 39, 941-948.

Radha, A.V., Navrotsky, A., 2013. Thermodynamics of carbonates. Reviews in Mineralogy & Geochemistry 77, 73-121.

Renaut, R.W., Jones, B., 1997. Controls on aragonite and calcite precipitation in hot spring travertines at Chemurkeu, Lake Bogoria, Kenya. Canadian Journal of Earth Sciences 34, 801-814.

Romanek, C.S., Grossman, E.L., Morse, J.W., 1992. Carbon isotope fractionation in synthetic aragonite and calcite: Effects of temperature and precipitation rate. Geochimica et Cosmochimica Acta 56, 419-430.

Scheuer, G., Schweitzer, F., 1985. Types and forms of travertine cones. Földtani Kőzlőny, Bulletin of the Hungarian Geological Society 115, 385-398 [in Hungarian with English summary].

Sharp, Z., 2007. Principles of Stable Isotope Geochemistry. Pearson Prentice Hall, New Jersey, 334 p.

Speer, J.A., Hensley-Dunn, M.L., 1976. Strontianite composition and physical properties. American Mineralogist 61, 1001-1004.

Suganuma, I., 1928. On the constituents and genesis of a few minerals produced from hot springs and their vicinities in Japan. III. Calcium carbonate minerals deposited from effervescent springs. Bulletin of the Chemical Society of Japan 3, 87-89.

Takashima, C., Kano, A., Naganuma, T., Tazaki, K., 2008. Laminated iron texture by iron-oxidizing bacteria in a calcite travertine. Geomicrobiology Journal 25, 193-202.

Takashima, C., Okumura, T., Nishida, S., Koike, H., Kano, A., 2011. Bacterial symbiosis forming laminated iron-rich deposits in Okuoku-hachikurou hot spring, Akita Prefecture, Japan. Island Arc 20, p. 294-304.

Zhang, G., Liu, C., Liu, H., Jin, Z., Han, G., Li, L., 2008. Geochemistry of the Rehai and Ruidan geothermal waters, Yunnan Province, China. Geothermics 37, 73-83.

Zhou, X., Fang, B., Zhou, H., Li, L., Wang, Y., 2015. Isotopes of deuterium and oxygen-18 in thermal groundwater in China. Environmental Geology 57, 1807-1814.

Zhu, M., Tong, W., 1987. Surface hydrothermal minerals and their distribution in the Tengchong geothermal area, China. Geothermics 16, 181-195.

FIGURE CAPTIONS

Fig. 1. Location of study area. (A) Map showing location of Tengchong in western China, which is the closest city to the study area. (B) Location of Shiqiang (Stone Wall) and other spring sites around Tengchong. (C) Detailed map of Shaqiang (based on Google Earth and field mapping) showing location of spring towers (red). Samples used in this study came from ST1, ST2, and ST3.

Fig. 2. Spring towers in lake in northwest corner of Shiqiang (see Fig. 1C). (A) General view to southwest showing inactive spring towers, now overgrown with vegetation, in man-made lake. (B) View of cone-shaped tower with vent at apex. (C) View of mushroom-shaped tower with vent at apex. Sampling of these vents was not permitted.

Fig. 3. Spring towers in southeast part of Shiqiang. (A) General view of ST1 (see Fig. 1C), which is now inactive and covered with moss. Grass is rooted in soil that fills vent at apex. (B) General view of ST2 (see Fig. 1C) showing tree growing in soil that fills vent at top. (C) General view of lower side of ST1 showing alternating grey and orange layers. Note white precipitates in cavities. (D) Enlarged view of white precipitates (calcite and aragonite) partly filling open cavities. (E) View of small open, accessory vent near apex of ST1.

Fig. 4. Thin section photomicrographs showing general architecture of columns that characterize Phase I-A precipitates in ST1. Note lack of common pattern in the branching. A = aragonite; C = calcite. Blue = porosity. A-C and E with plane polarized light. (A) Column growing from round nucleus at base (possibly cross-section of poorly preserved twig), formed largely of calcite but with some aragonite. ST1, ~ 0.5 m above base. (B) Basal part of large column constructed of smaller columns that are formed of aragonite and calcite. White letter C indicates position of panel C. Base of ST1. (C) Enlarged view of column base showing

aragonite fans overlain by calcite. Base of ST1. (D) Same view as panel C but with cross polarized light. (E) Aragonite fan on top of calcite.

Fig. 5. SEM photomicrographs of columns that characterize Phase I precipitates in ST1 and ST2 (see Fig. 1C). (A) Array of irregular columns. ST1, ~ 0.6 m above base. White letter B indicates position of panel B. (B) Enlarged view of columns, showing irregular morphology. (C) General view of columns. ST1, ~ 0.5 m above base. White letter D indicates position of panel D. (D) Interior of column formed of leached calcite. White letter E indicates position of panel E. (E) Leached calcite from interior part of column. (F) Cross-section through vertical branch showing highly porous, leached calcite interior encased by thin calcite wall. ST1, 0.65 m above base. (G) Cross-section through two small columns with hollow interiors. White letter H indicates position of panel H. ST2, ~ 0.3 m above base. (H) Leached interior and outer calcite wall.

Fig. 6. Thin section photomicrographs showing relationships between the calcite and Fe-rich precipitates. (A) Alternating laminae of calcite with Fe-dendrites (white layers) and Fe-rich laminae (dark brown layers). Sample from side vent near top of ST1. Plane polarized light. (B) Laminae formed of Fe-dendrites (dark brown to black) embedded in calcite (white). Upper part of ST1, around main vent. Plane polarized light. (C) Same view as panel B but with crossed polarized light.

Fig. 7. SEM photomicrographs of Fe precipitates associated with calcite in ST1 and ST2. (A) Clusters of needle-shaped Fe-rich crystals nestled between calcite crystals. ST1, 0.6 m above base. 8A and 8B indicate positions of EDX analyses shown in Fig. 8A, B, respectively. (B) Calcite crystal surrounded by Fe-rich crystals. ST1, 0.6 m above base. (C) Calcite crystals with numerous open round to ovate bodies defined by Fe-rich crystals. ST1,

0.65 m above base. 8C and 8D indicate positions of EDX analyses shown in Fig. 8C, D, respectively. (D) Hollow spheres with walls formed of Fe-rich crystals. ST1, 0.65 m above base. (E) Cluster of laminated spheres formed of Fe-rich precipitates. ST2, ~0.1 m above base. (F) Cluster of hollow spheres formed of Fe-rich precipitates. ST2, ~0.1 m above base.

Fig. 8. EDX analyses from calcite and Fe-rich precipitates shown in Figure 7A (A and B) and 7C (C and D), respectively.

Fig. 9. Thin section photomicrographs of zoned calcite crystals with alternating Fe-rich (brown) and Fe-poor (white) zones. Blue = porosity. All with plane polarized light. All from ST2, ~ 0.2 m above base. (A) General view of zoned calcite crystals held in spar calcite cement. (B) Group of zoned euhedral calcite crystals held in Fe-rich calcite cement. (C) Zoned euhedral calcite crystal with partly leached interior (blue).

Fig. 10. SEM photomicrographs of partly leached calcite crystals. All from ST1, 0.6 m above base. (A) Zoning in calcite crystal accentuated by dissolution of some zones. (B) Zoned calcite crystal with dissolution of some zones. (C) Zoned calcite crystals with selective dissolution of some zones.

Fig. 11. Thin section photomicrographs of coated grains from ST1. All with plane polarized light. Blue = porosity. Coated grains in panels A-E and H-I came from pool deposits around main vent at top of ST1. Coated grain shown in panels F and G is isolated specimen from precipitates at tower base. (A-E) Coated grains with variable architectures defined by aragonite and Fe-rich cortical laminae (brown). (F, G) Coated grain formed of alternating calcite and Fe-rich laminae. Isolated specimen found among calcite columns at base of ST1. Panel G is enlargement from upper right quadrant of coated grain shown in panel F. (H, I)

Fe coated grains from deposits around main vent of ST1. Panel I, which is an enlargement of central part of panel H, shows details of cortical laminae.

Fig. 12. Thin section photomicrographs of calcite rafts from pool deposits around main vent of ST1. All with plane polarized light. (A) Group of rafts with calcite on underside (top rafts) or both sides (bottom raft). (B) Group of rafts, each with calcite crystals growing from all sides. White letter C indicates position of panel C. (C) Ends of rafts showing calcite crystals radiating outwards from all surfaces.

Fig. 13. Thin section photomicrographs of Phase II precipitates, all with plane polarized light except for panels E and H. Panels A, B, D, and E from sample from close to top vent; panel C from sample from basal part of tower; panels F-H from sample ~ 0.25 m below top vent. Blue = porosity. (A) Cavity lined with isopachous calcite cement. (B) Cavities filled with aragonite cements. (C) Cavity filled with laterally linked aragonite fans. (D) Linked aragonite fans in bottom part of cavity overlain by calcite cement. (E) Same view as panel D but with crossed polarized light. (F) Cavity with linked aragonite fans at base. (G) Enlarged view from central part of panel F showing laterally linked aragonite fans. Note color contrast between inner and outer parts of the fans. (H) Same view as panel G but with crossed polarized light.

Fig. 14. SEM photomicrographs of Phase II aragonite and associated precipitates. Panels A and B from basal part of ST1; C and D from around vent pool, upper part of ST1, and E and F from basal part of ST3. (A) Oblique view of aragonite fan showing radiating crystals. (B) Enlarged view of upper right corner of panel A showing distal parts of aragonite crystals. (C) Cross-sections through cluster of aragonite crystals. (D) Oblique view of crystal faces of aragonite crystals with zig-zag suture lines (arrows) that are indicative of cyclic twinning.

(E) Upper part laterally merged aragonite fans overlain by thin layer formed of fibrous crystals. 15A and 15B indicate positions of EDX analyses shown in Figure 15A and B, respectively. (F) Enlarged view of fibrous crystals that form thin layer shown in panel E. EDX analyses show that they are formed of Ca and Sr (Fig. 15B) whereas the underlying aragonite crystals are formed of Ca.

Fig. 15. EDX analyses of points 15A and 15B shown in Figure 14E. The high Sr and low Ba peaks for 15B indicate that the fibrous crystals are strontianite.

Fig. 16. SEM photomicrographs showing aragonite, strontianite, and associated precipitates that form part of the Phase II cements. Sample from basal part of ST3. Panels B, E, F, and H are BSE images with the dark bands formed of Ca and light bands formed of Ca, Sr, and Ba. (A) General view of precipitates showing locations of EDX analyses shown in Figure 17A and 17B and area shown in panel B (white box labeled B). (B) BSE image showing contrast between aragonite (dark) and zones with high Ca, Sr, and Ba content. White letters E and G indicate position of panels E and G, respectively. (C) Outer part of crust formed of intercalated aragonite and strontianite. White letter D indicates position of panel D. (D) Enlarged view of crust showing locations of EDX analyses shown in Figure 17C, 17D, 17E. (E, F) SEM views of outer crust shown in panel B. Panel F is BSE image with dark colored bands being formed of Ca and the light colored bands containing Ca, Sr, and Ba. (G, H) SEM and BSE image of outer crust shown in panel B with BSE image highlighting zones with high content of Ca, Sr, and Ba. Panel G shows locations of EDX analyses shown in Figure 17F to K.

Fig. 17. EDX analyses of spots shown in Figure 16.

1090 **Fig. 18.** SEM photomicrographs of reticulate Mg-Si coatings associated with Phase II aragonite
1091 cements like those shown in Fig. 13C, D, and F. Sample from lower part of ST1. C = calcite.
1092 (A) Reticulate Mg-Si coating covering aragonite substrate. Note calcite crystals on top of
1093 the reticulate coating. 19A indicates position of EDX analysis shown in Figure 19A. (B)
1094 Enlarged view of reticulate coating. White letter C indicates position of panel C. (C) Calcite
1095 cement filling voids between Si-Mg plates in the Mg-Si reticulate coating. (D) Cavity lined
1096 with complex succession of Mg-Si reticulate coatings. White letter E indicates position of
1097 panel E. (E) Two layers of reticulate Mg-Si coating with second layer showing plate-like
1098 form of the coating. 19B indicates position of EDX analysis shown in Figure 19B. (F)
1099 Oblique view of reticulate coating. 19C indicates position of EDX analysis shown in Figure
1100 19C. (G) Isolated masses of Mg-Si reticulate coating on top of aragonite cement. White H
1101 indicates position of panel H. 19D indicates position of EDX analysis shown in Fig. 19D.
1102 (H) Enlarged view of reticulate coating shown in panel G. 19E indicates position of EDX
1103 analysis shown in Fig. 19E. (I) Broken sections through Mg-Si reticular coatings. 19F, 19G,
1104 and 19H indicate positions of EDX analyses shown in Figure 19G, H, and I, respectively.
1105 **Fig. 19.** EDX analyses of points shown in Figure 18.
1106 **Fig. 20.** SEM photomicrographs of late stage calcite cements associated with Phase III
1107 precipitation. These cements lie on top of aragonite cement. All samples from lower part of
1108 ST1. (A) General view of cement formed of nested trigonal calcite crystals. (B) Enlarged
1109 view of surface of cement shown in panel A showing nested trigonal calcite crystals. (C, D)
1110 Oblique view of vertical fracture through calcite cement formed of upward expanding
1111 clusters of nested trigonal crystals. (E, F) Unattached euhedral dodecahedral calcite crystals,
1112 with beveled crystal edges, resting on top of earlier formed aragonite and/or calcite cements.

Fig. 21. (A) Surfaces of columns covered with needle-fiber calcite crystals that formed during phase III precipitation. (B) Densely packed needle-fiber crystals of various morphologies that completely disguise the host substrate.

Fig. 22. SEM photomicrographs showing micro-organisms, insects, calcified filamentous microbes, and microborings associated with Phase III. (A) Non-calcified filamentous microbe. Base of ST3. (B, C) Non-calcified filamentous microbes interwoven with needle-fiber calcite crystals. ~ 0.65 m > base of ST1. (D) Diatom frustules. Near top of ST1. (E) Well-preserved euglypharid with calcareous plates. Base of T3. (F) Insect lodged between calcite crystals. ~ 0.5 m > base of ST1. (G, H) Calcified *Syctonema julianum*. ~ 0.25 m below top of ST1. (I) Calcified reticulate filament. ~ 0.6 m > base of ST1. (J, K) Calcified filaments. ~ 0.5 m > base of ST1. (L-N) Microborings in calcite crystals. Note remnants of formative microbes in borings in panel N.

Fig. 23. Thin section photomicrographs showing partial dissolution of aragonite and calcite that forms parts of the columns. All with plane polarized light. Blue = porosity. (A) Aragonite fan in basal part of column with interior that has been largely lost due to dissolution. ST1, 0.5 m above base. (B) Neighboring aragonite fans from basal part of column showing irregular and varied degrees of internal dissolution. ST1, 0.5 m above base. (C) Vertical cross-section through column showing internal calcite crystals with hollow cores. Crystals held in spar calcite cement (white). ST1, 0.6 m above base. (D) Cross-section through column formed largely of extensively leached crystals. ST1, 0.6 m above base. (E) Cluster of hollow euhedral calcite crystals from central part of a column. ST1, base of tower.

Fig. 24. SEM photomicrographs showing alteration of Phase II aragonite cements. A-E from sample at base of ST1; panels F-L from sample from base of T3. (A) General view of

surface of laterally linked lobes formed of aragonite needle cement. (B) Vertical cross-section through aragonite cement shown in panel A. Note bundles of radiating crystals that at low-magnification appear to be formed of aragonite. White letter C indicates position of panel C. (C) Enlarged view of cement shown in panel B. White letters D and E indicate positions of panels D and E, respectively. (D) Lower part of cement, from panel C, that is formed of very small, loosely interlocking crystals that are < 1 μm long. (E) Upper part of cement shown in panel C. Note increased porosity in uppermost part of crust. (F) General view of radiating aragonite (?) crystals. White letter G indicates position of panel G. (G) Enlarged view showing interlocking irregular-shaped crystals. (H) Cross-section through aragonite (?) cement with growth line. Different part of sample from that shown in panel F. White letter I indicates position of panel I. (I) Enlarged view from panel H showing small constituent crystals. White letter J indicates position of panel J. (J) Enlarged view of constituent crystals. (K) Groups of aragonite (A) crystals encased by calcite (C). (L) Aragonite crystals (A) with no evidence of alteration embedded in calcite (C).

Fig. 25. Bivariant graph showing relationships between $\delta^{18}O_{SMOW}$ and $\delta^{13}C_{PDB}$ for samples from ST1, ST2, and ST3 relative to samples from the two modern springs S1 and S2 (from Jones and Peng, in press). Note samples from the towers plot into two distinct groups, largely on the basis of significant differences in their $\delta^{13}C_{PDB}$ values. The numbers indicate the position of the samples in each tower and B (brown) and W (white) refers to the color of the sample in the hand sample, which corresponds to Phase I and Phase II precipitates, respectively.

Fig. 26. Comparison of the $\delta^{18}O_{SMOW}$ and $\delta^{13}C_{PDB}$ for samples from the spring towers at Shiqiang relative to spring deposits elsewhere in the Yunnan Province (data from Jones and Peng, 2012, 2014d, 2014b, in press) and the Kenyan Rift Valley (data from Renaut and

Jones, 1997). Note that Group A from Shiqiang plots along the same trend line as for the other springs in Yunnan whereas Group B from Shiqiang does not follow that trend line.

Fig. 27. Comparison of water temperatures calculated from $\delta^{18}O$ using the equations of Anderson and Arthur (1983), Hays and Grossman (1991), Kim and O'Neil (1997), O'Neil et al. (1969), and Chacko and Deines (2008). All calculations used a $\delta^{18}O_{(water)}$ value of -11‰, which is the value derived from the waters from the modern spring S1 and S2 by Jones and Peng (2016).

Fig. 28. Comparison of $\delta^{13}C_{PDB}$ in carrier CO_2 as determined from the equations by Panichi and Tongiorgi (1976), Romanek et al. (1992), Emrich et al. (1970), and Chacko et al. (2001). Values derived from the Chacko et al. (2001) equation, stressed by the large green circle, are the ones used in this study.

Figure 1

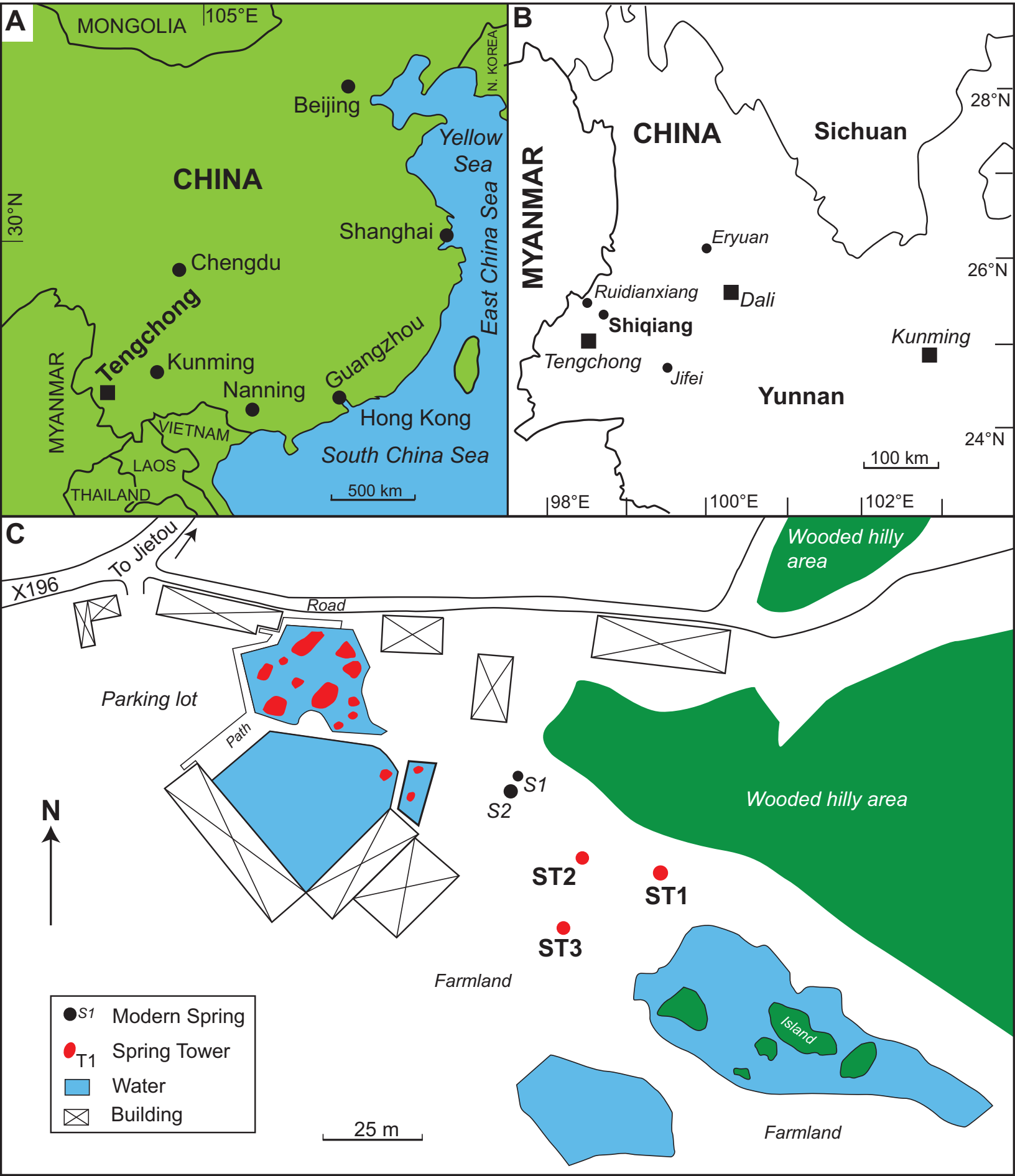
A
MONGOLIA
105°E
N. KOREA
Beijing
Yellow Sea
CHINA
30°N
Shanghai
East China Sea
Chengdu
Tengchong
Kunming
Guangzhou
Nanning
MYANMAR
VIETNAM
Hong Kong
LAOS
South China Sea
THAILAND
500 km
B
CHINA
Sichuan
28°N
MYANMAR
Eryuan
26°N
Ruidianxiang
Dali
Shiqiang
Kunming
Tengchong
Jifei
Yunnan
24°N
100 km
98°E
100°E
102°E
C
To Jietou
X196
Road
Wooded hilly area
Parking lot
Path
S1
S2
N
Wooded hilly area
ST2
ST1
ST3
Farmland
Island
Modern Spring
Spring Tower
Water
Building
25 m
Farmland

Figure 2
Click here to download high resolution image

Figure 3
Click here to download high resolution image

Figure 4
Click here to download high resolution image

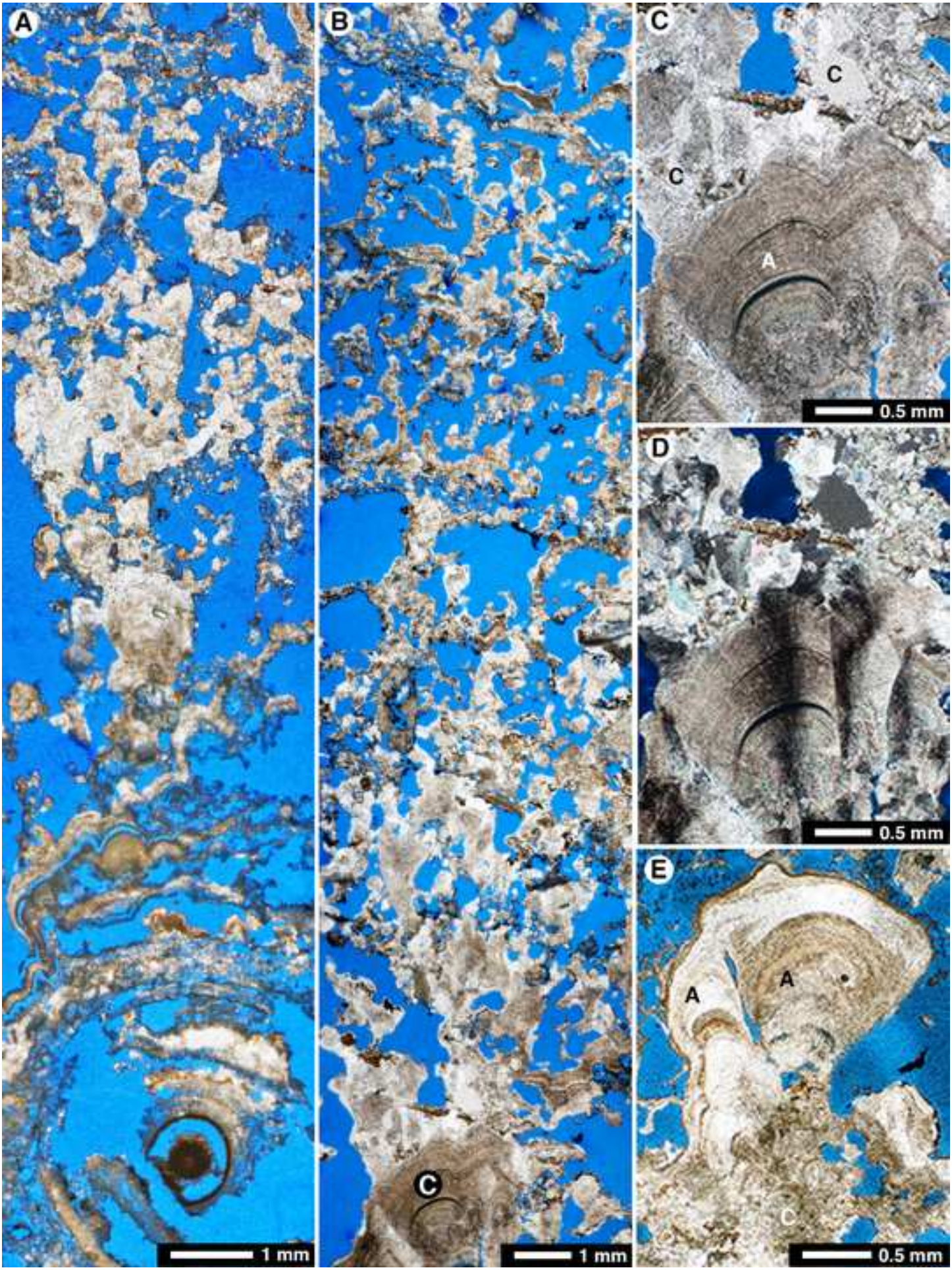

Figure 5
Click here to download high resolution image

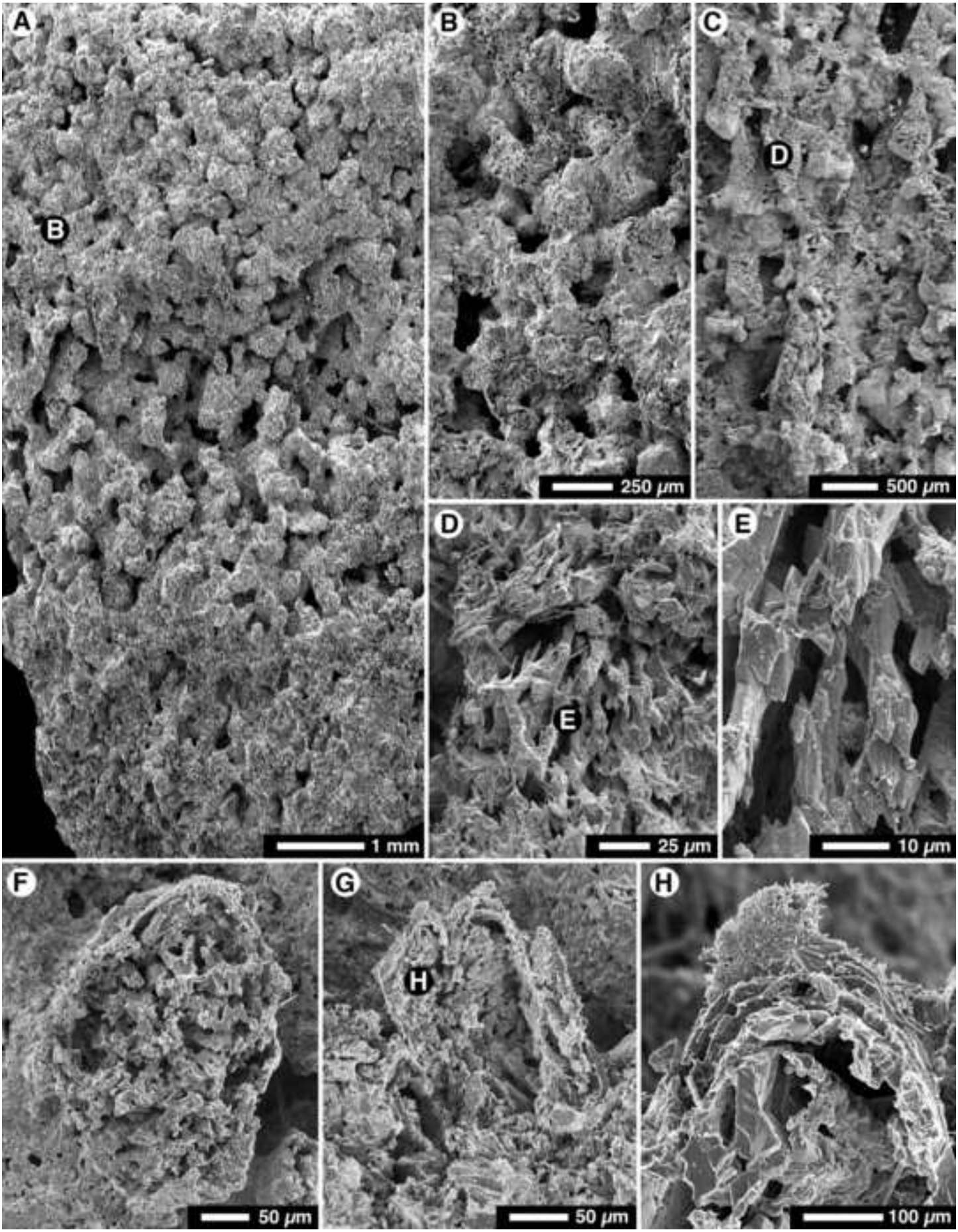

Figure 6
Click here to download high resolution image

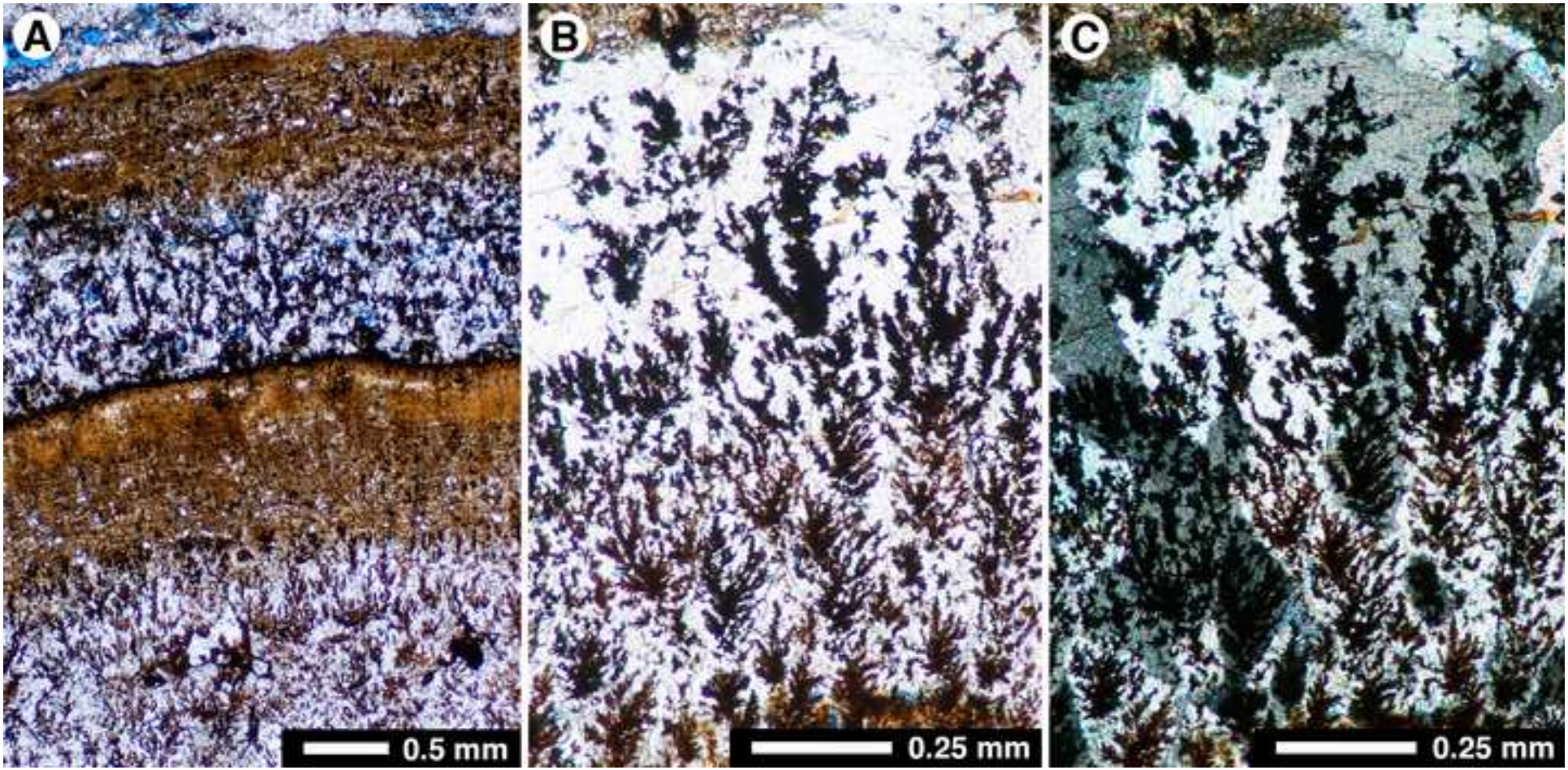

Figure 7
Click here to download high resolution image

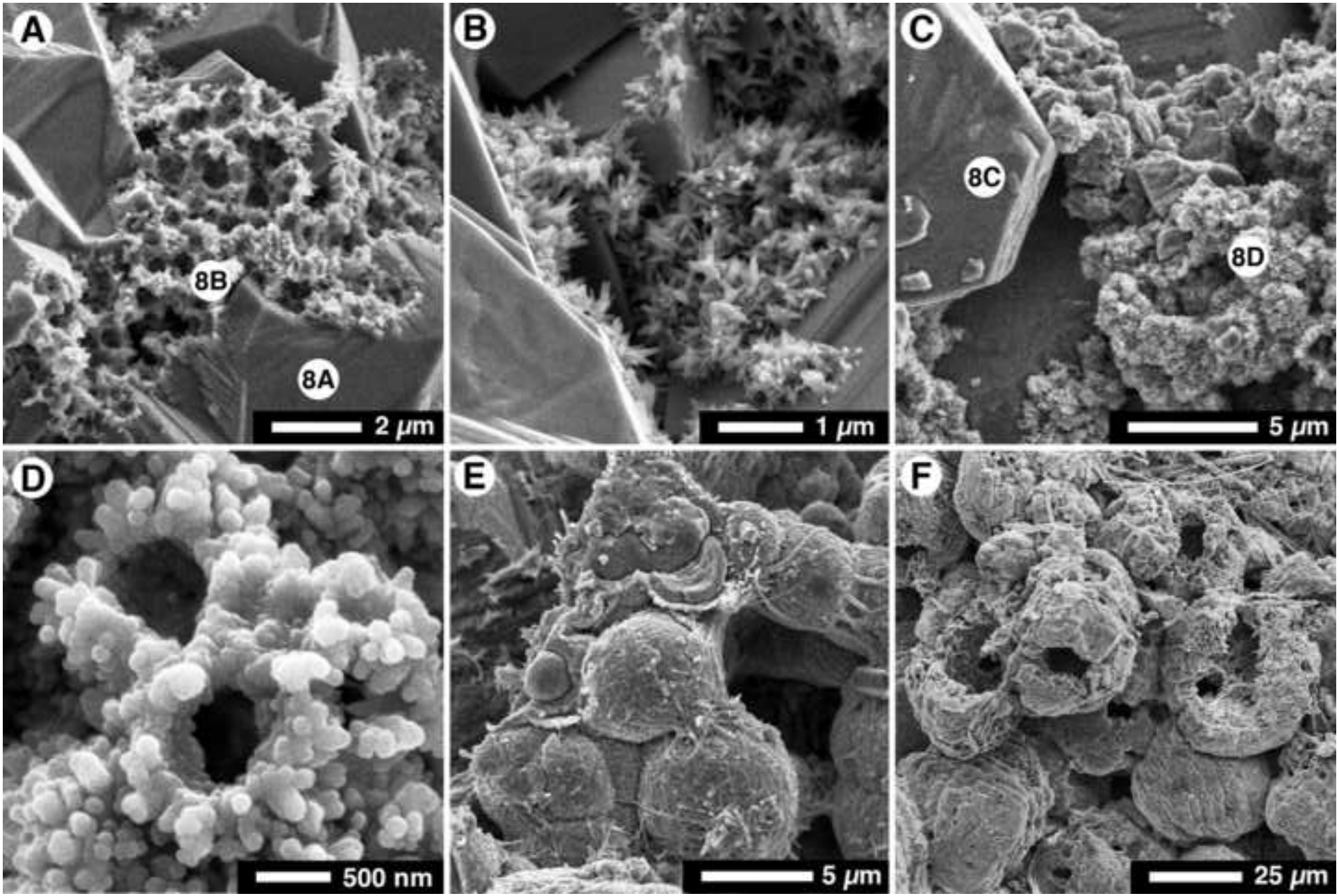

Figure 8

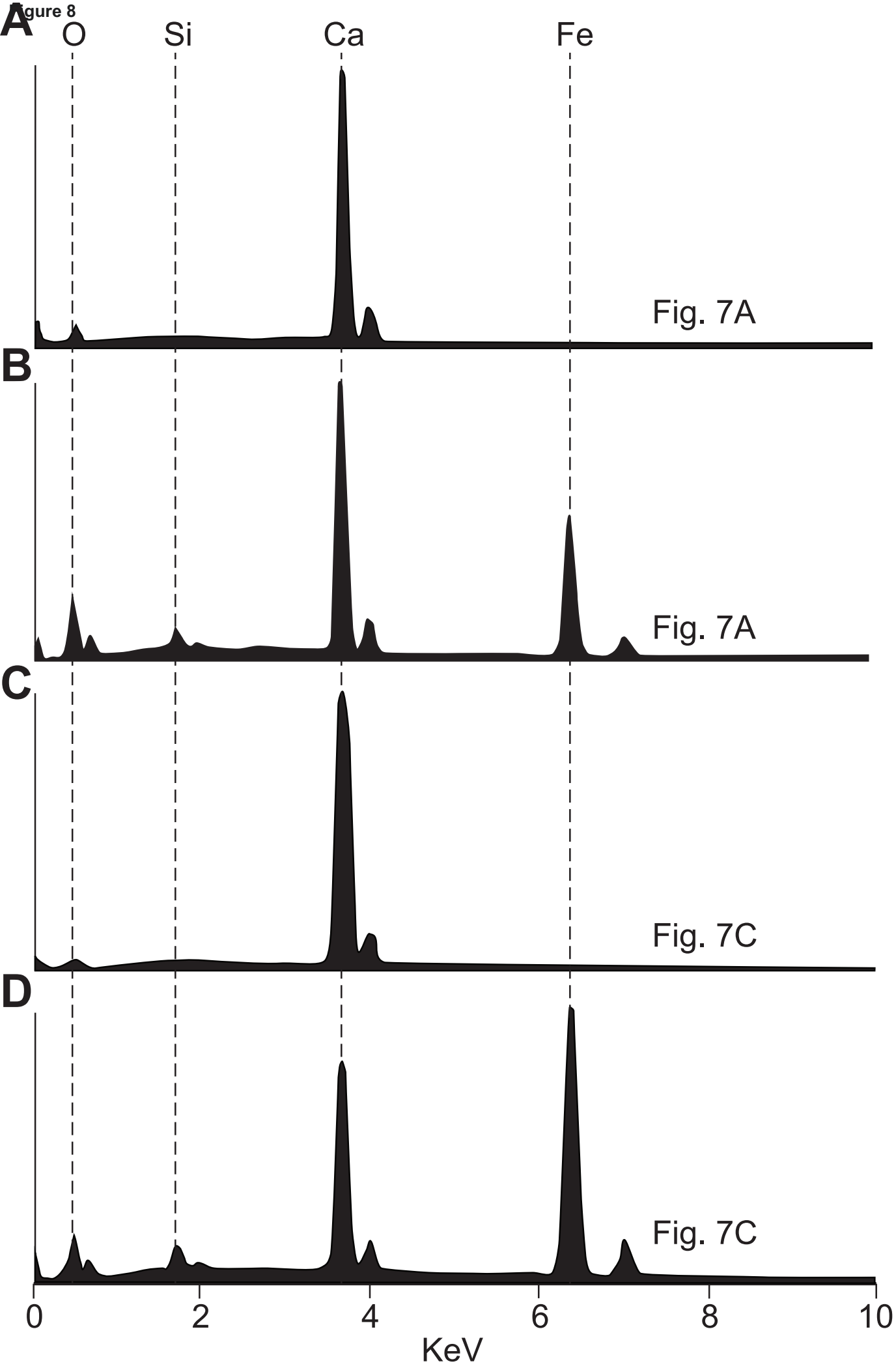

Figure 9
Click here to download high resolution image

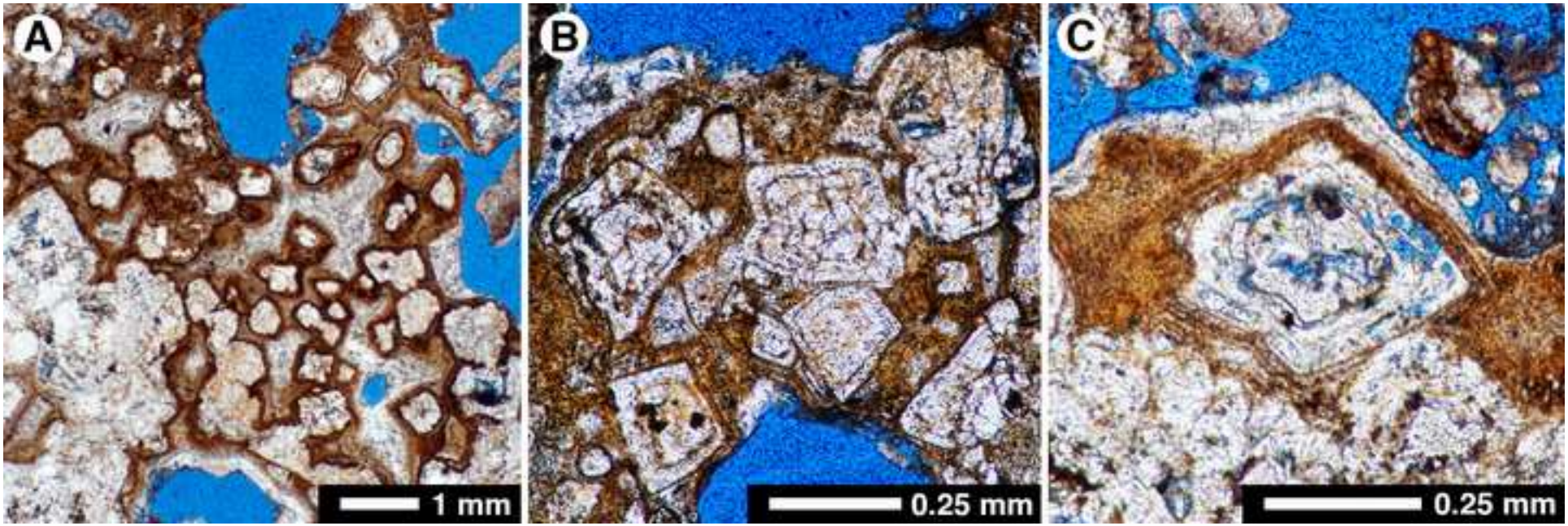

Figure 10
Click here to download high resolution image

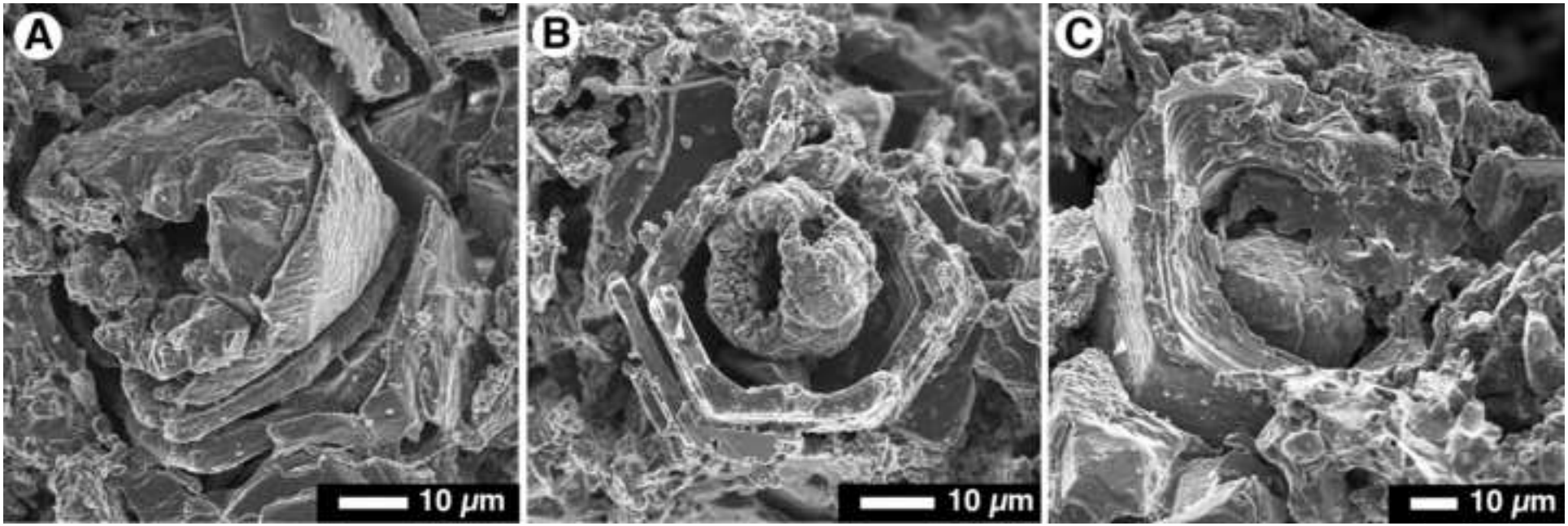

Figure 11
Click here to download high resolution image

Figure 12
Click here to download high resolution image

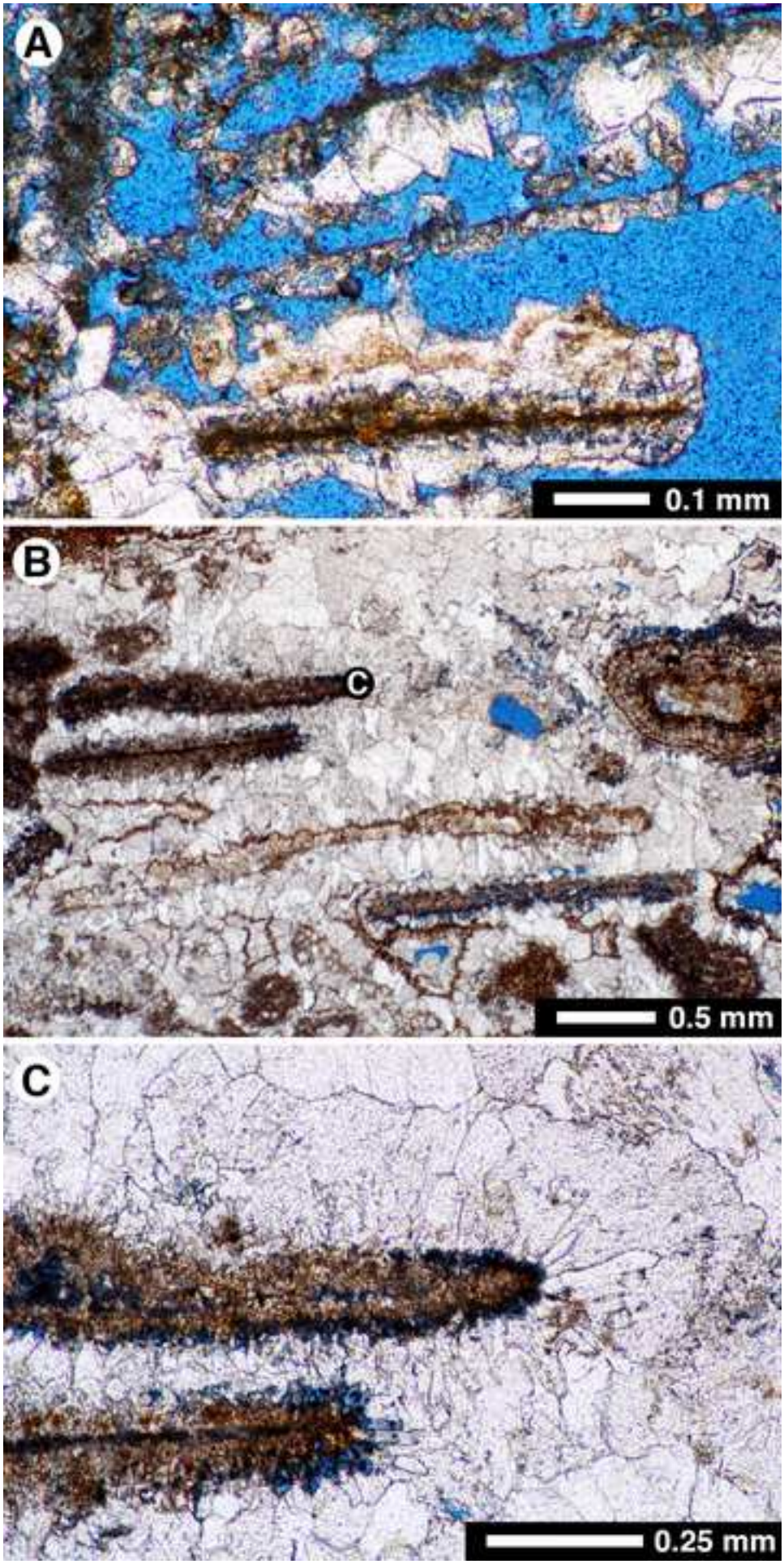

Figure 13
Click here to download high resolution image

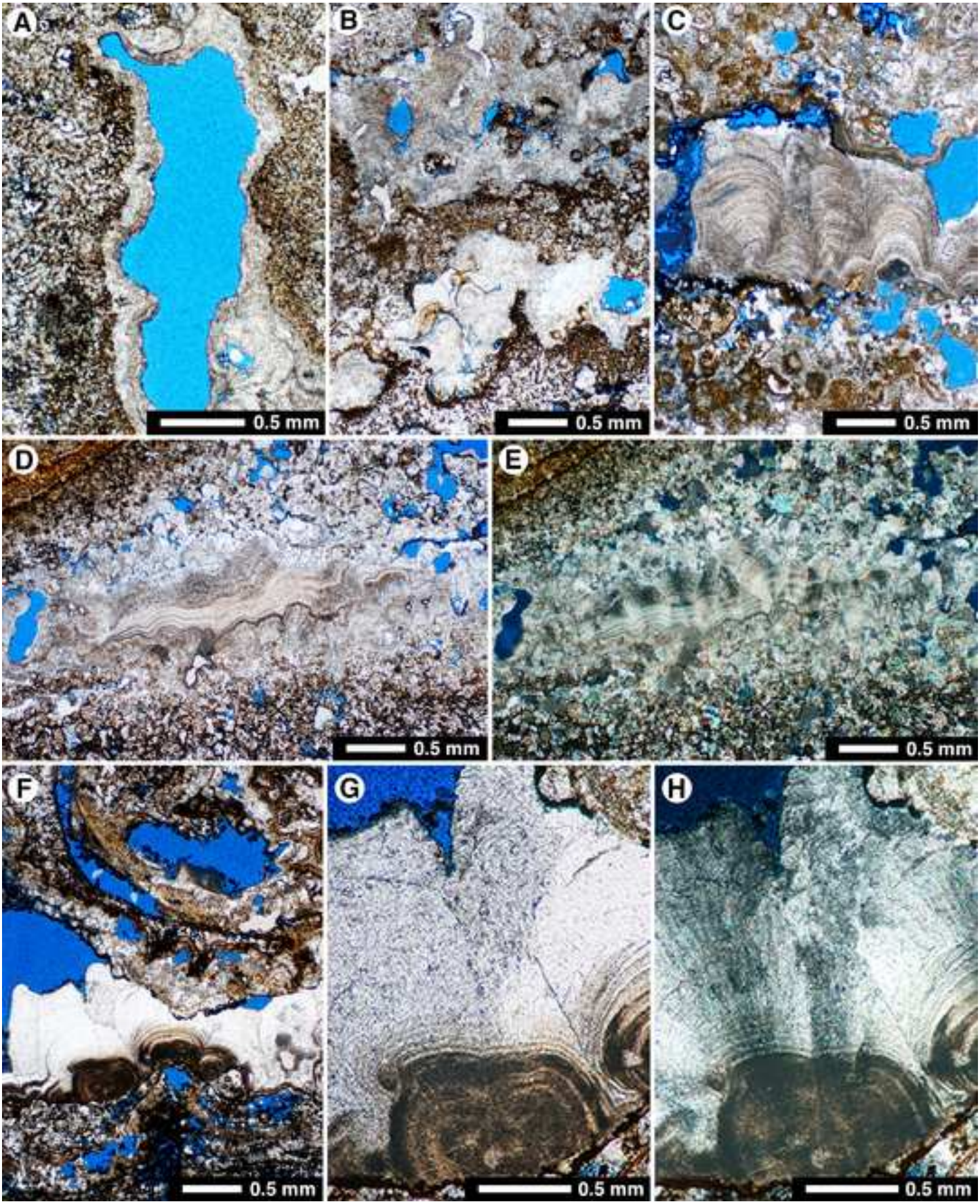

Figure 14
Click here to download high resolution image

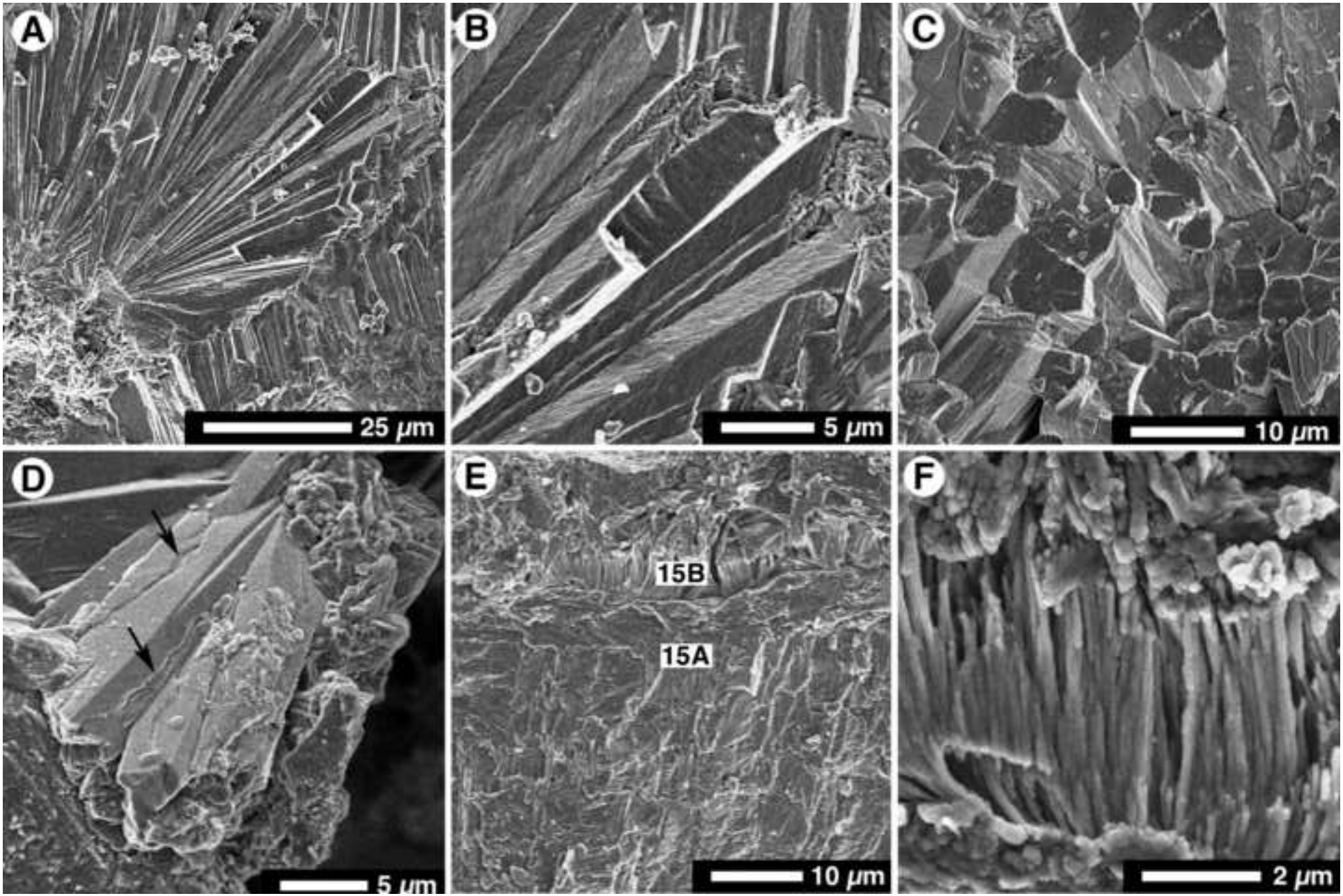

Figure 15

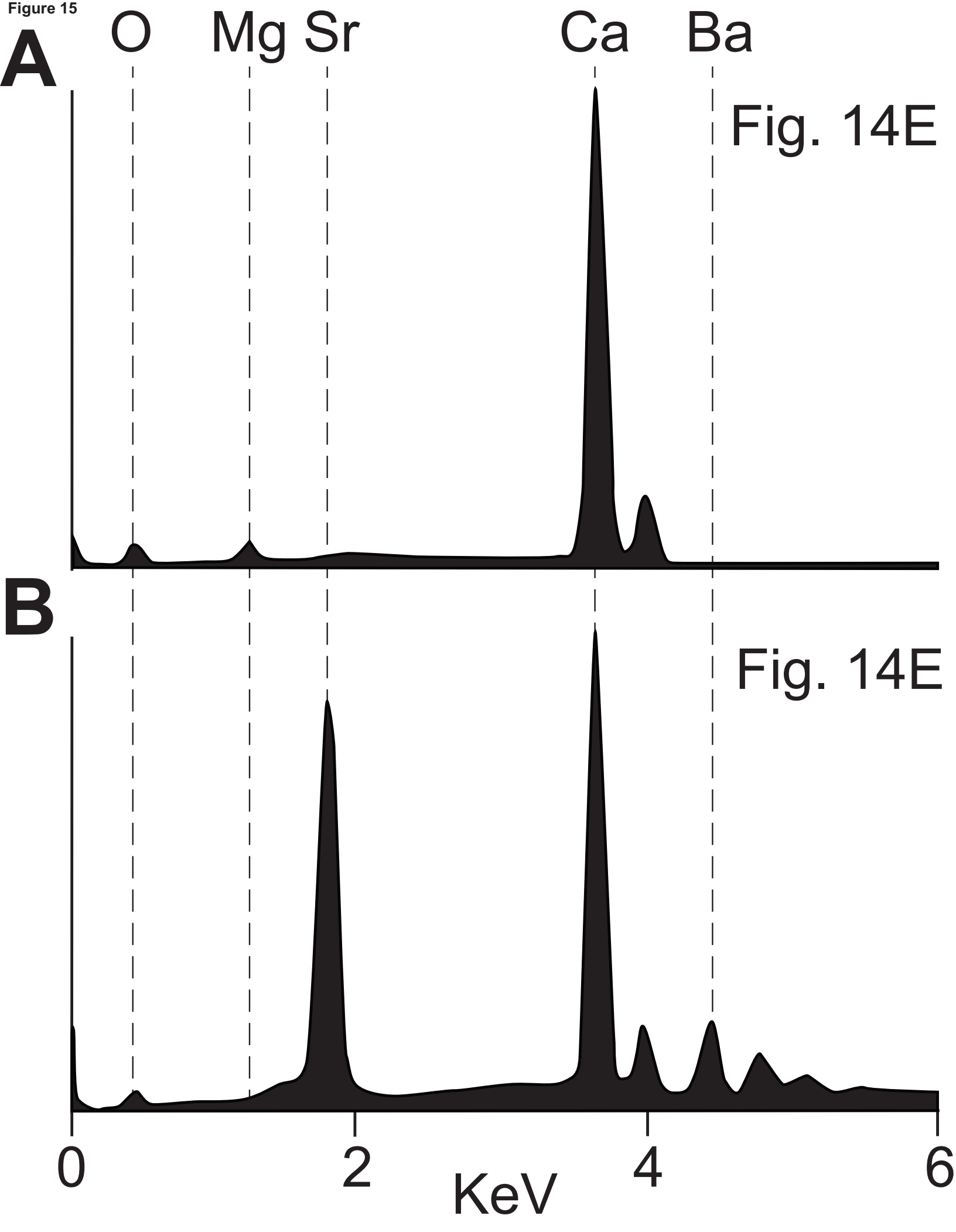

Figure 16
Click here to download high resolution image

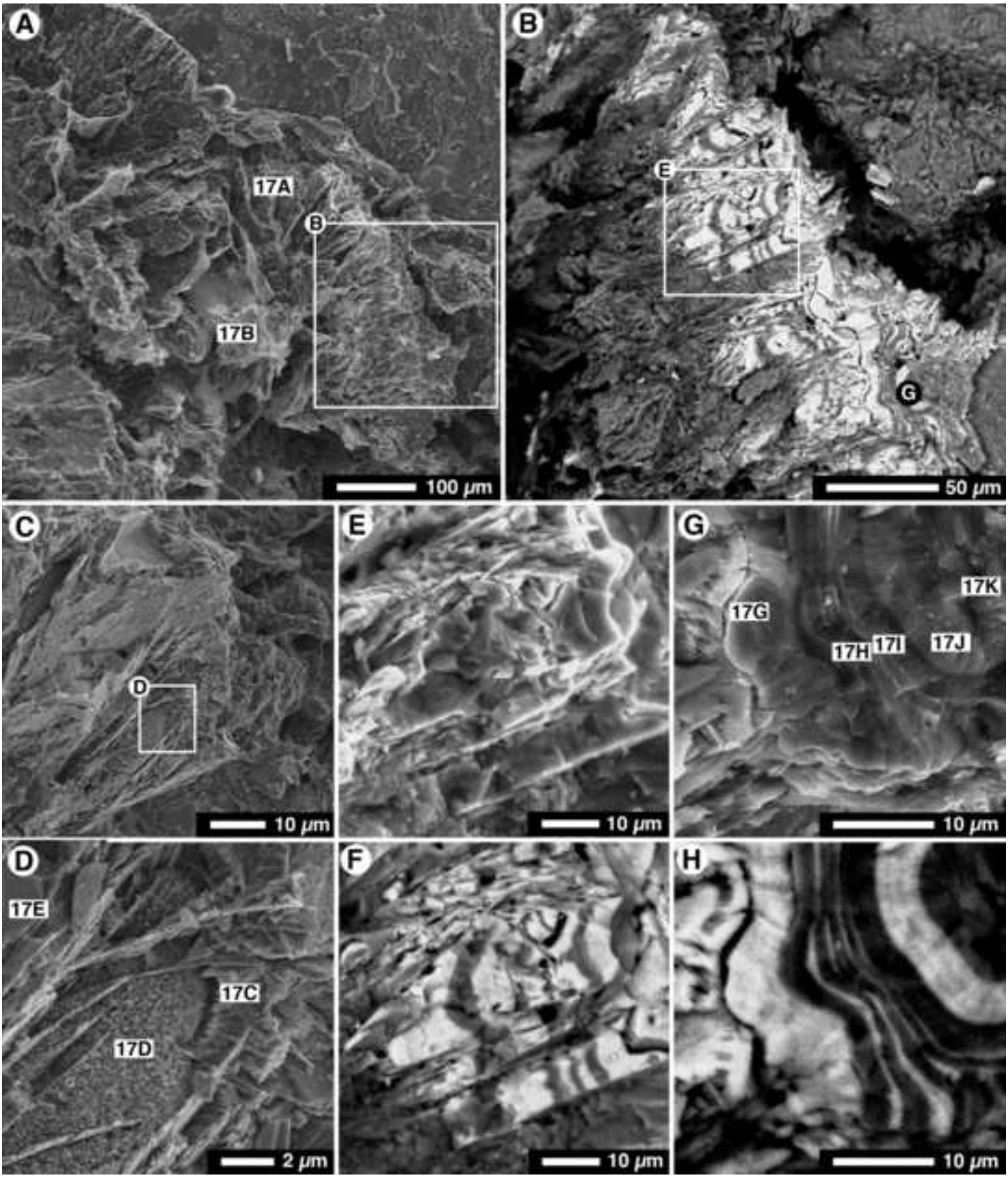

Figure 17

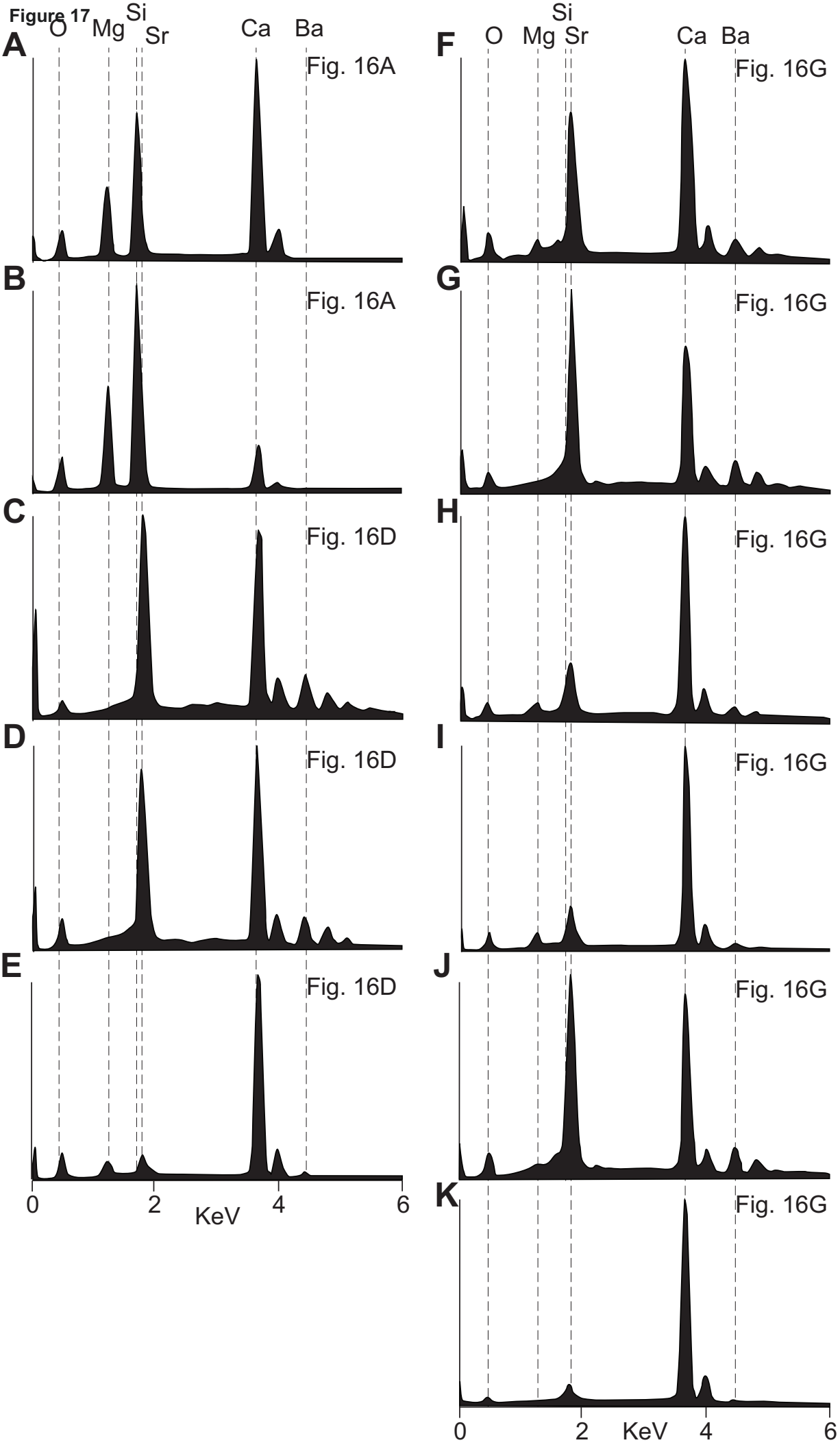
A
O
Mg
Si
Sr
Ca
Ba
Fig. 16A
B
Fig. 16A
C
Fig. 16D
D
Fig. 16D
E
Fig. 16D
0
2
4
6
KeV
F
O
Mg
Si
Sr
Ca
Ba
Fig. 16G
G
Fig. 16G
H
Fig. 16G
I
Fig. 16G
J
Fig. 16G
K
Fig. 16G
0
2
KeV
4
6

Figure 18
Click here to download high resolution image

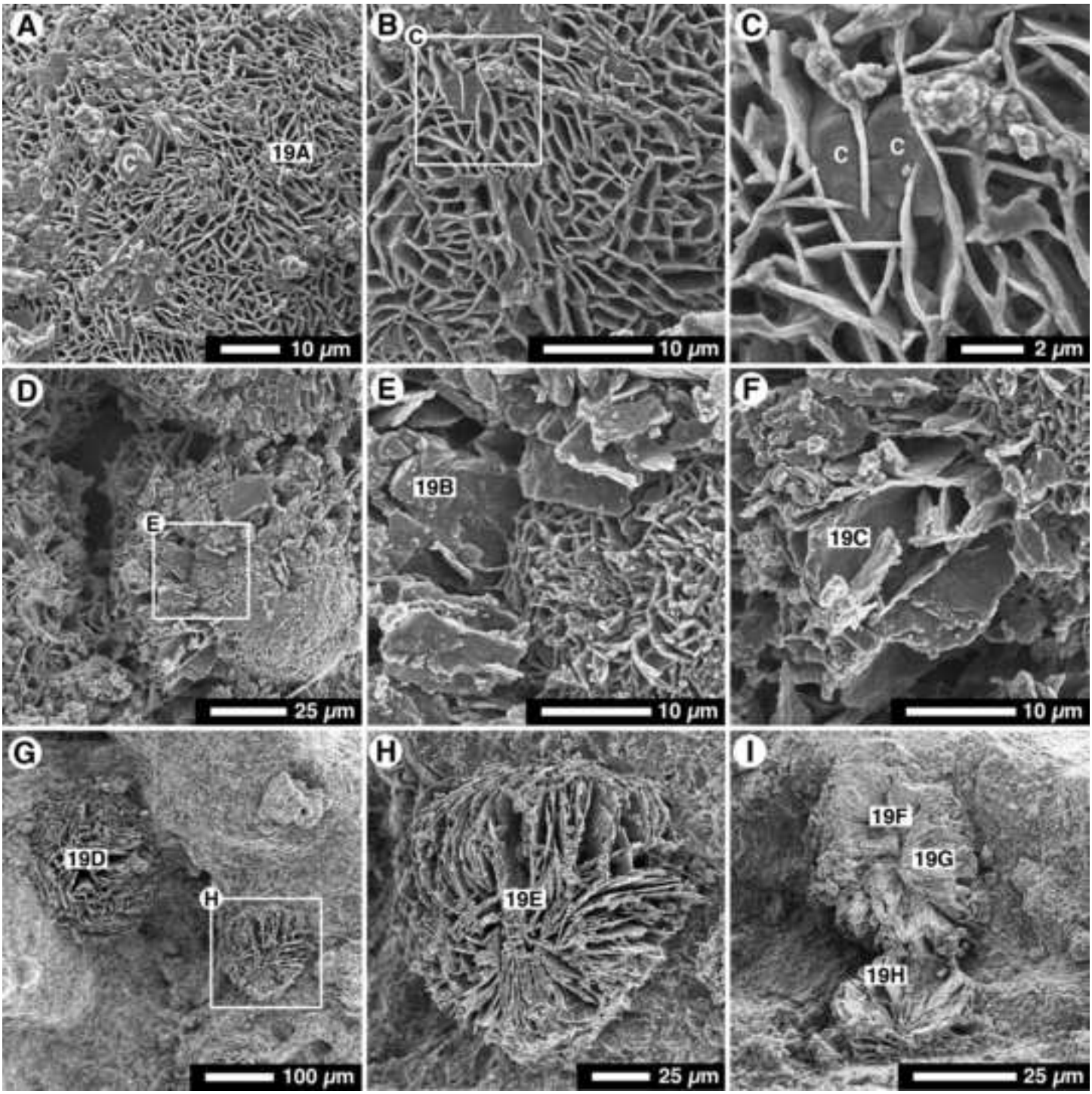

Figure 19

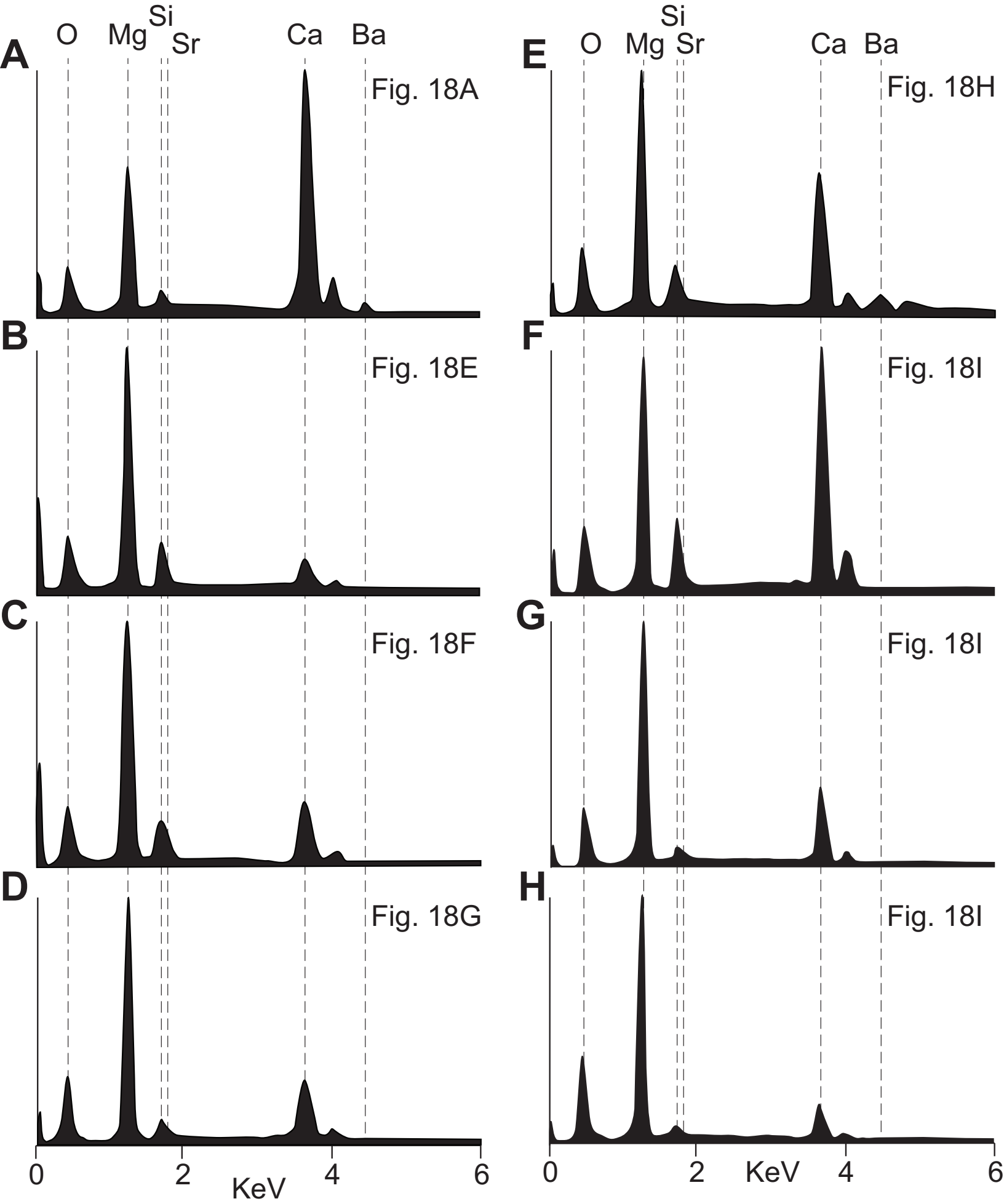
A
O
Mg
Si
Sr
Ca
Ba
Fig. 18A
B
Fig. 18E
C
Fig. 18F
D
Fig. 18G
0
2
4
6
KeV
E
O
Mg
Si
Sr
Ca
Ba
Fig. 18H
F
Fig. 18I
G
Fig. 18I
H
Fig. 18I
0
2
4
6
KeV

Figure 20
Click here to download high resolution image

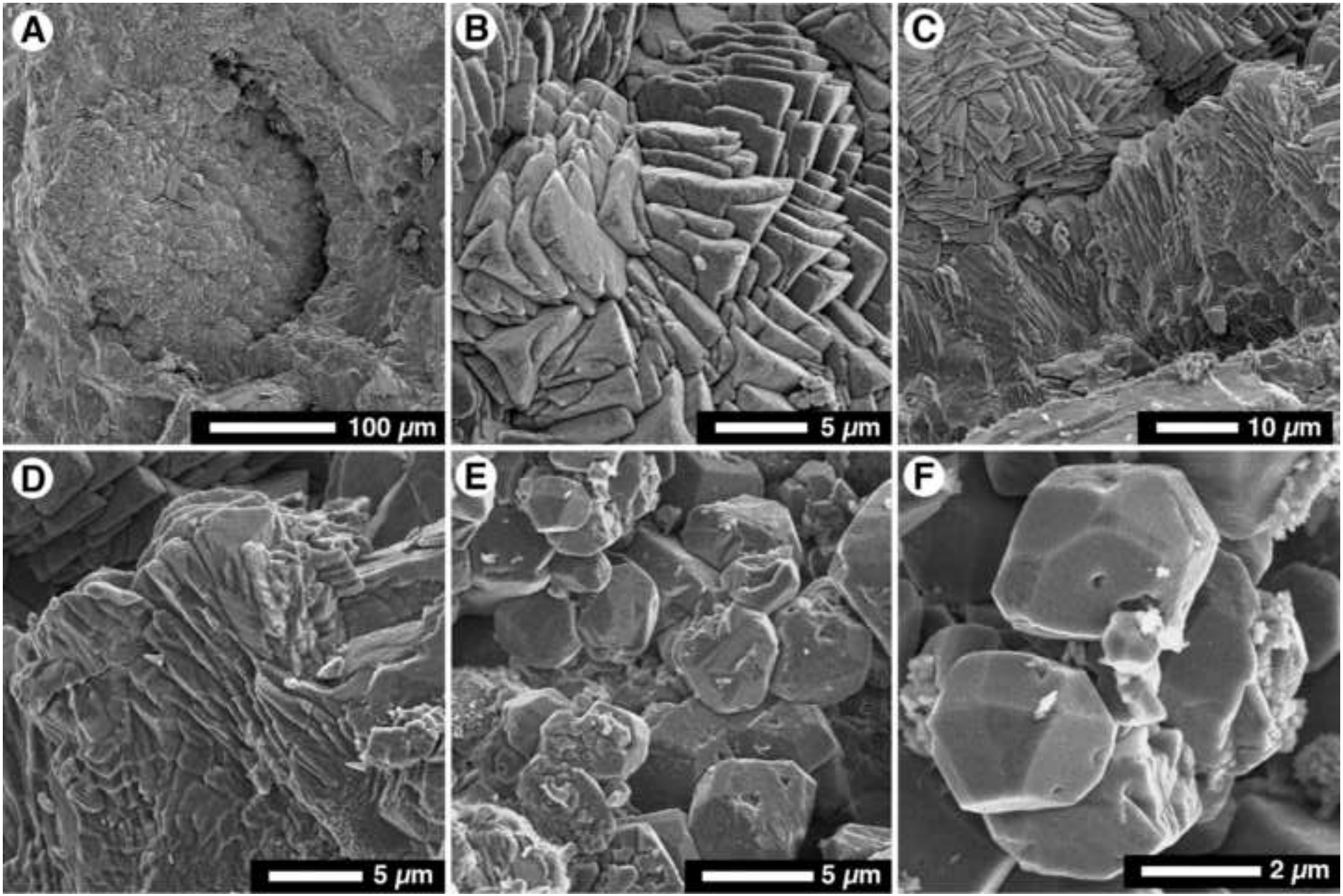

Figure 21
Click here to download high resolution image

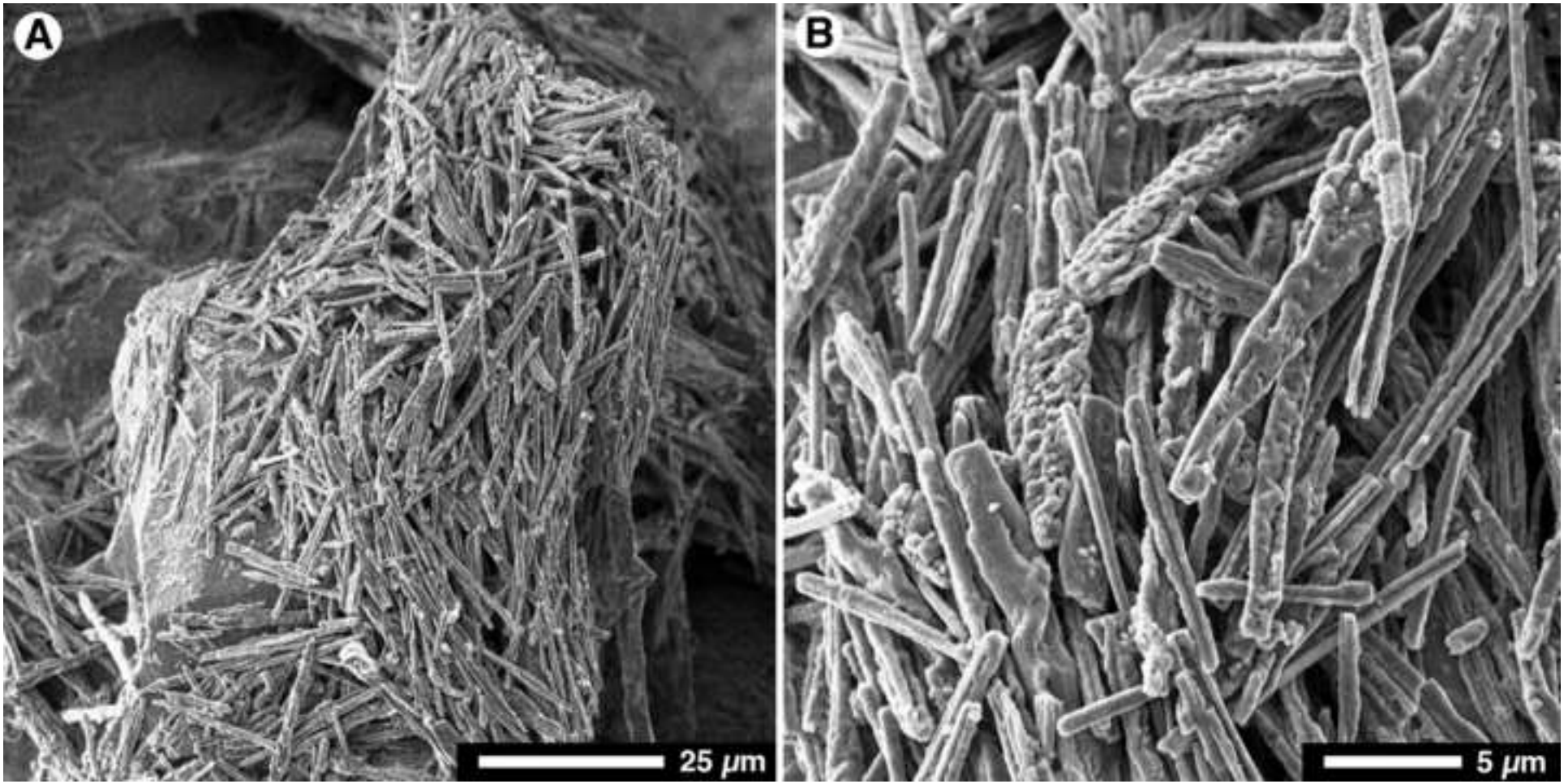

Figure 22
Click here to download high resolution image

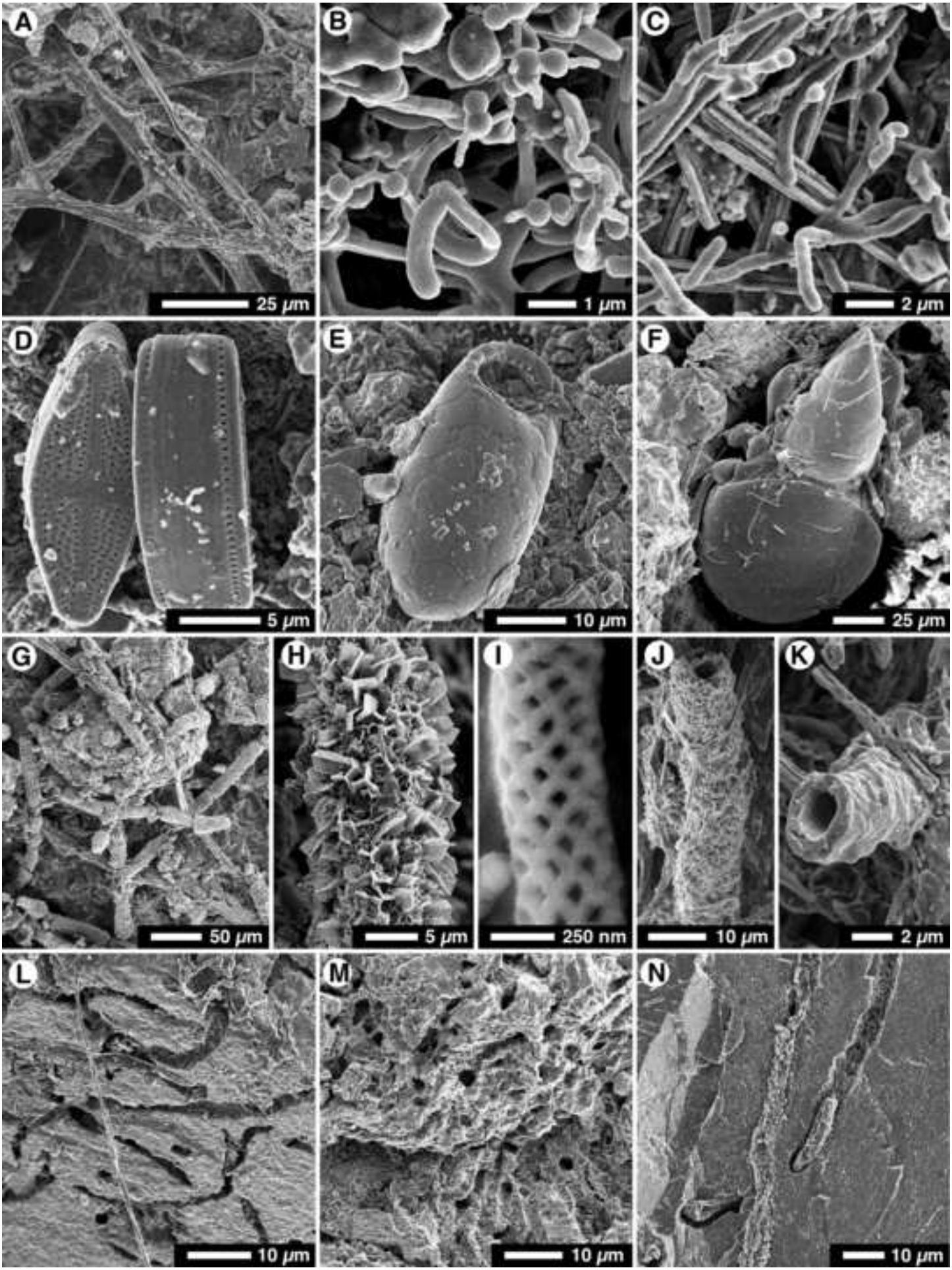

Figure 23
Click here to download high resolution image

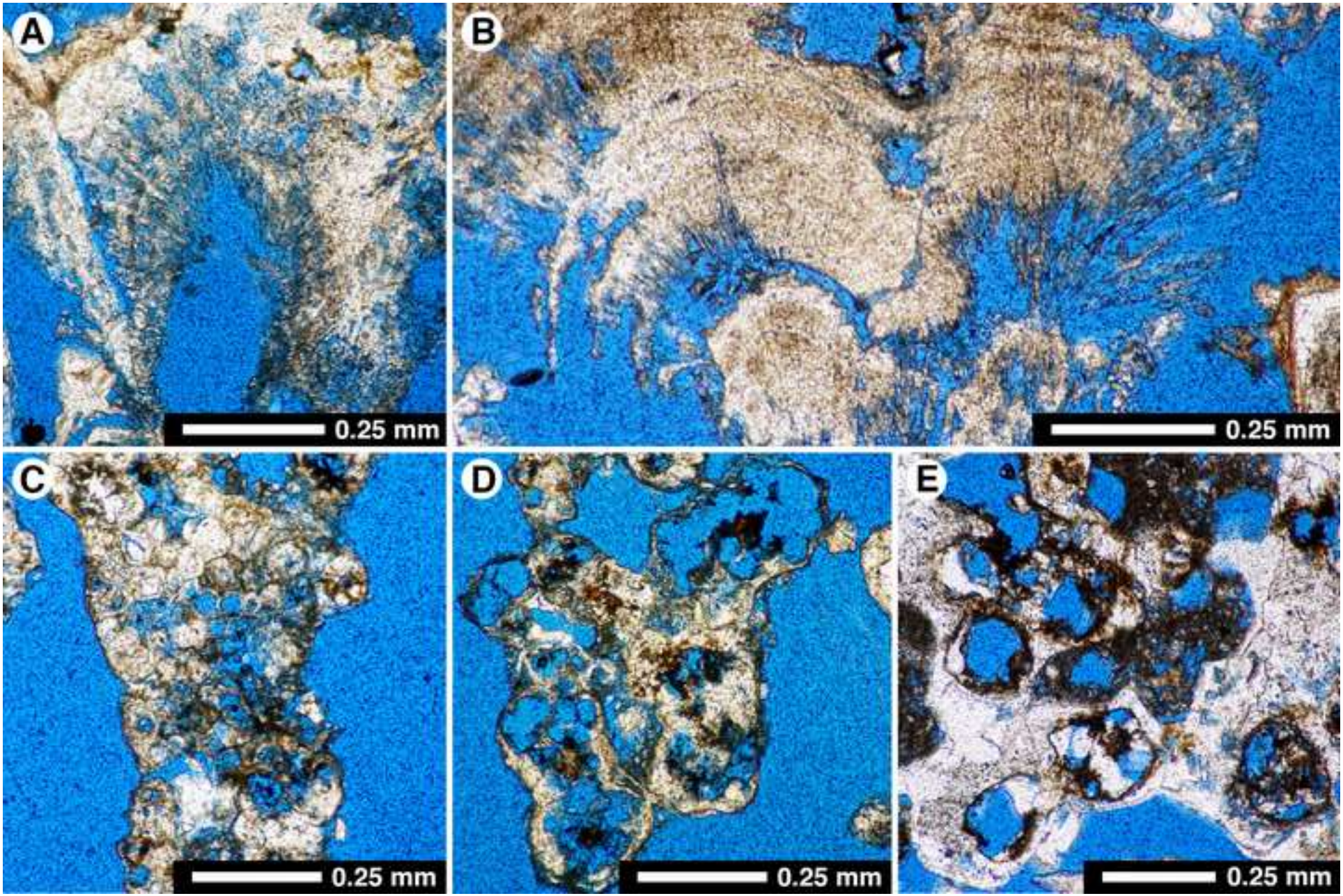

Figure 24
Click here to download high resolution image

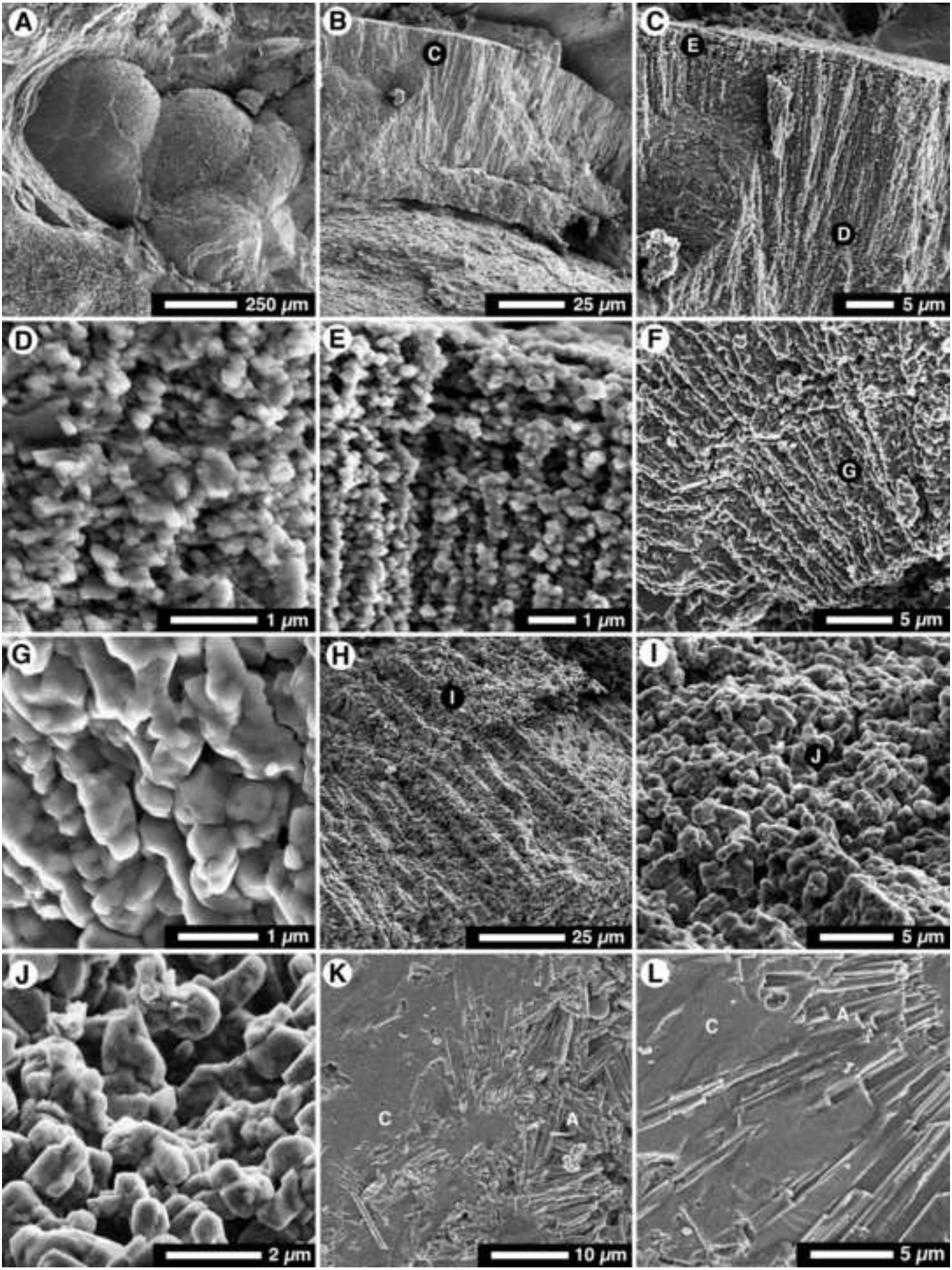

Figure 25

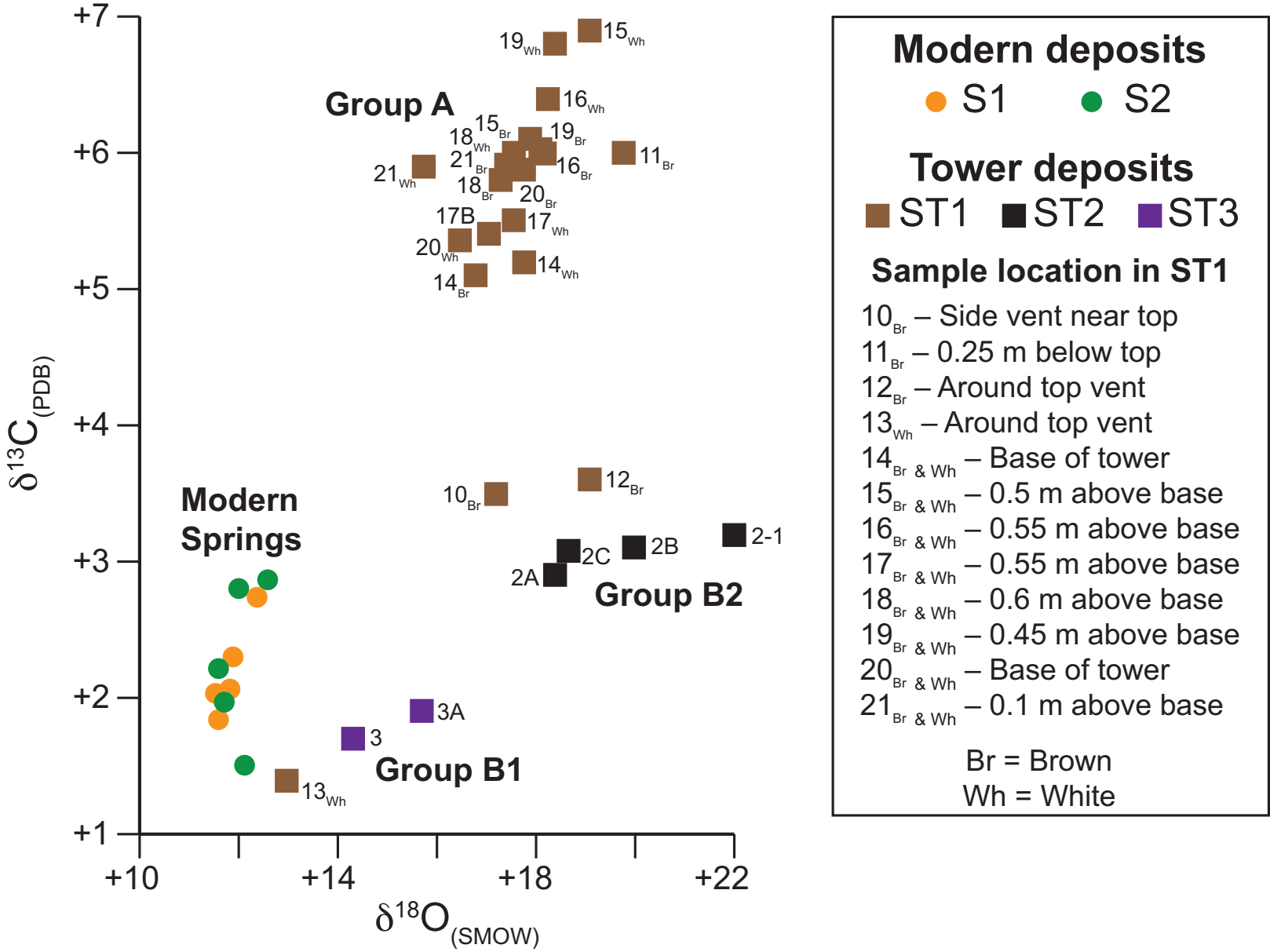
+7
+6
+5
+4
+3
+2
+1
+10
+14
+18
+22
δ13C (PDB)
δ18O (SMOW)
Group A
Modern Springs
Group B1
Group B2
19Wh
15Wh
16Wh
15Br
18Wh
19Br
21Br
16Br
11Br
21Wh
18Br
20Br
17B
17Wh
20Wh
14Wh
14Br
10Br
12Br
2-1
2C
2B
2A
3A
3
13Wh
Modern deposits
S1
S2
Tower deposits
ST1
ST2
ST3
Sample location in ST1
10Br – Side vent near top
11Br – 0.25 m below top
12Br – Around top vent
13Wh – Around top vent
14Br & Wh – Base of tower
15Br & Wh – 0.5 m above base
16Br & Wh – 0.55 m above base
17Br & Wh – 0.55 m above base
18Br & Wh – 0.6 m above base
19Br & Wh – 0.45 m above base
20Br & Wh – Base of tower
21Br & Wh – 0.1 m above base
Br = Brown
Wh = White

Figure 26

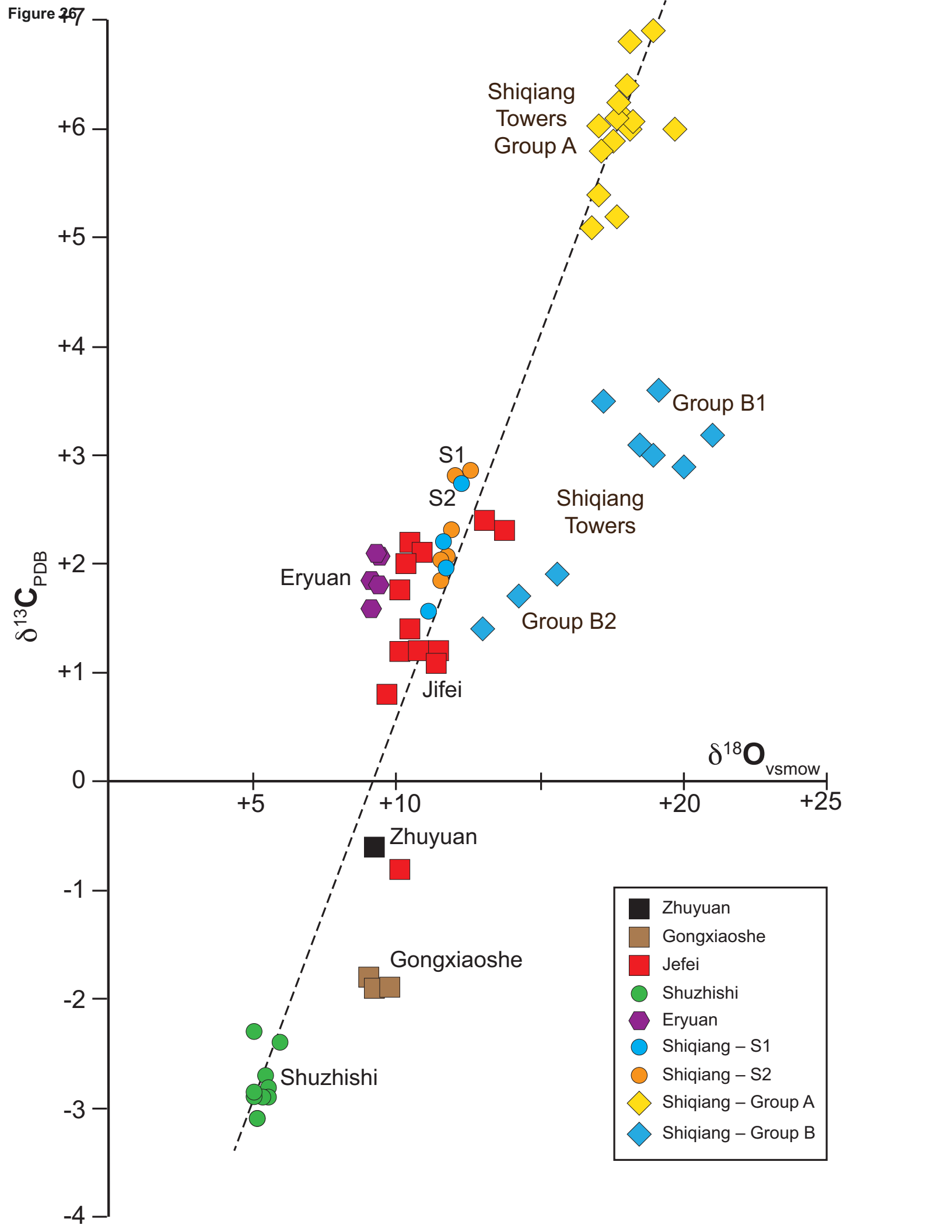
+7
+6
+5
+4
+3
+2
+1
0
-1
-2
-3
-4
δ13CPDB
+5
+10
+20
+25
δ18Ovsmow
Shiqiang
Towers
Group A
Group B1
S1
S2
Shiqiang
Towers
Eryuan
Group B2
Jifei
Zhuyuan
Gongxiaoshe
Shuzhishi
Zhuyuan
Gongxiaoshe
Jefei
Shuzhishi
Eryuan
Shiqiang – S1
Shiqiang – S2
Shiqiang – Group A
Shiqiang – Group B

Figure 27

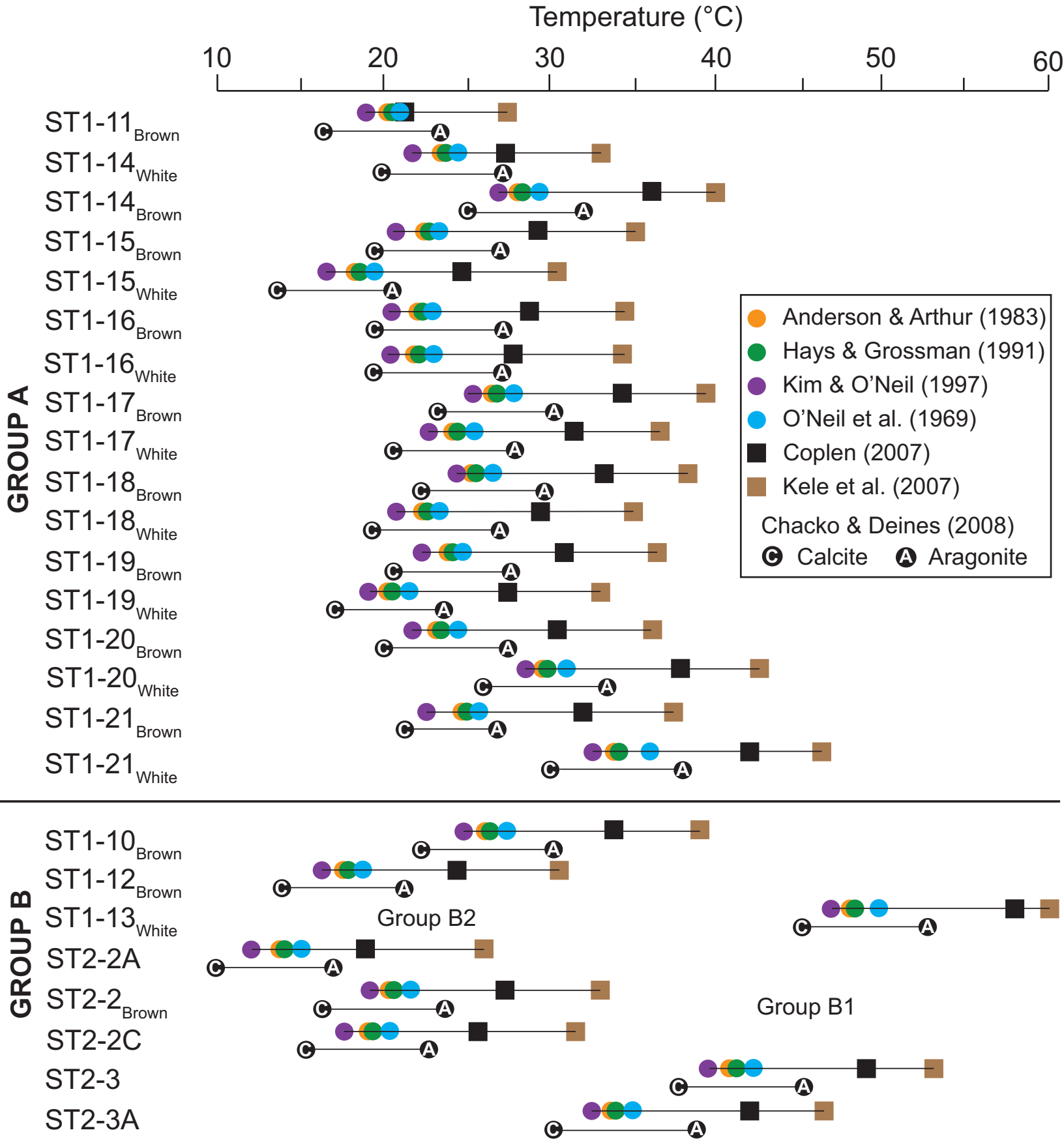
Temperature (°C)
10
20
30
40
50
60
GROUP A
ST1-11 Brown
ST1-14 White
ST1-14 Brown
ST1-15 Brown
ST1-15 White
ST1-16 Brown
ST1-16 White
ST1-17 Brown
ST1-17 White
ST1-18 Brown
ST1-18 White
ST1-19 Brown
ST1-19 White
ST1-20 Brown
ST1-20 White
ST1-21 Brown
ST1-21 White
Anderson & Arthur (1983)
Hays & Grossman (1991)
Kim & O'Neil (1997)
O'Neil et al. (1969)
Coplen (2007)
Kele et al. (2007)
Chacko & Deines (2008)
C Calcite
A Aragonite
GROUP B
ST1-10 Brown
ST1-12 Brown
ST1-13 White
ST2-2A
ST2-2 Brown
ST2-2C
ST2-3
ST2-3A
Group B2
Group B1

Figure 28

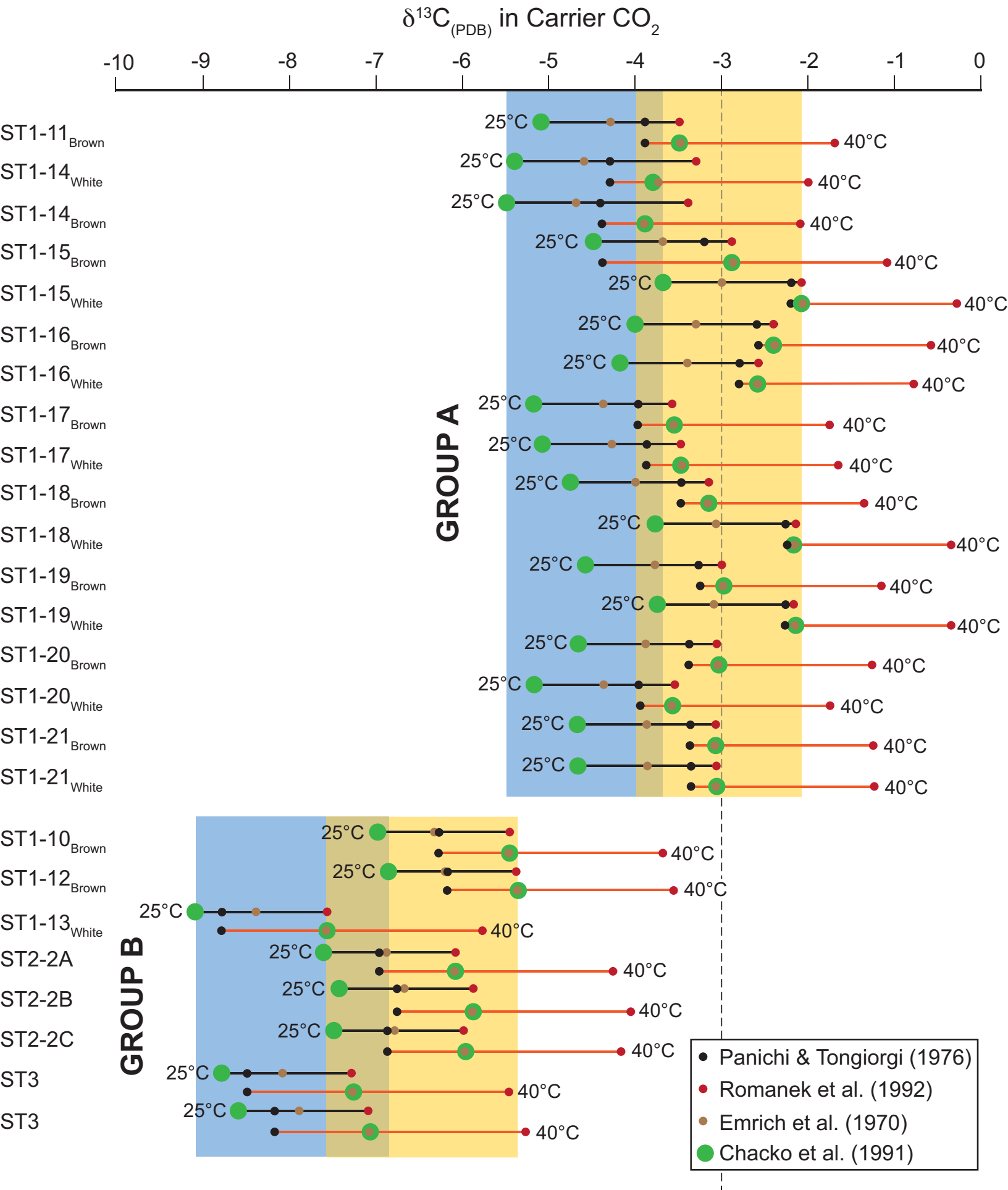
δ13C(PDB) in Carrier CO2
-10
-9
-8
-7
-6
-5
-4
-3
-2
-1
0
GROUP A
GROUP B
ST1-11Brown
ST1-14White
ST1-14Brown
ST1-15Brown
ST1-15White
ST1-16Brown
ST1-16White
ST1-17Brown
ST1-17White
ST1-18Brown
ST1-18White
ST1-19Brown
ST1-19White
ST1-20Brown
ST1-20White
ST1-21Brown
ST1-21White
ST1-10Brown
ST1-12Brown
ST1-13White
ST2-2A
ST2-2B
ST2-2C
ST3
ST3
25°C
40°C
Panichi & Tongiorgi (1976)
Romanek et al. (1992)
Emrich et al. (1970)
Chacko et al. (1991)